UNIVERSIDAD TECNICA
FEDERICO SANTA MARIA

Departamento de Obras Civiles

3D NUMERICAL ANALYSIS OF PILE-SUPPORTED EXCAVATIONS UNDER BIDIRECTIONAL SEISMIC LOADING

Master's Thesis by

Belén Noemí Llanquilef Navarro

Submitted in partial fulfillment of the requirements for the degree of:

Master of Science in Civil Engineering

Advisor
Javier Ubilla Villagrán

October 2024

THESIS TITLE:

3D NUMERICAL ANALYSIS OF PILE-SUPPORTED EXCAVATIONS UNDER BIDIRECTIONAL SEISMIC LOADING

AUTHOR:

BELÉN NOEMÍ LLANQUILEF NAVARRO

THESIS PAPER, presented as a partial requirement to obtain the degree of MASTER OF CIVIL ENGINEERING SCIENCES at the Universidad Técnica Federico Santa María.

Name Advisor .....

Name Member 1 Commission .....

Name Member 2 Commission .....

Santiago, Chile, October 2024

NUMERICAL STATIC ANALYSIS IN A PILE-SUPPORTED EXCAVATION.

Belén Llanquilef Navarro[1], Javier Ubilla Villagrán[1]

[1] UTFSM.

Abstract

Discontinuous anchored piling support systems are frequently utilized in temporary deep excavations in Santiago de Chile due to the geological conditions characterized by stiff gravelly soil and a deep groundwater table. This research presents a comprehensive study involving the development of a 3D model to simulate such excavations supported by discontinuous anchored piles. The HS-Small constitutive model is employed to accurately replicate the properties of Santiago's gravel soil, the HS-Small constitutive model is employed, with parameters calibrated based on geophysical and laboratory experiments from previous research.

The main objective of this study is to conduct a dynamic analysis utilizing two Ricker wavelets and seismic waves, applied in two directions. This analysis aims to simulate real-world seismic events and assess the structural integrity of support systems under such conditions. The study employs advanced computational techniques to model these systems' behavior accurately. Additionally, the results from these dynamic analyses are compared with Chilean standards to evaluate the performance of the support systems. This comparison is essential to determine whether the standards are conservative and to ensure that the systems meet the required safety and performance criteria.

The findings derived from the dynamic analyses and the comparison with the Chilean standards offer valuable insights into the behavior and effectiveness of discontinuous anchored piling support systems under dynamic loading conditions. The results indicate that corner piles experience lower displacements and internal forces, but higher soil thrust. Additionally, the dynamically induced soil pressures in some scenarios exceed those calculated by the standards, highlighting areas for potential improvement in design practices.

Keywords: temporary deep excavations, 3D excavation modeling, dynamic analysis.

Table of Contents

List of Figures

List of Tables

1 Introduction

Currently, one of the main challenges in large cities is population growth, which has promoted the construction of buildings that are adjacent to others. Therefore, it is necessary to guarantee the stability of surrounding structures that could be affected during temporary vertical excavations. In this way, one of the most used methods in Santiago de Chile is the use of discontinuous anchored pile support as a retaining system due to the outstanding mechanical properties of the Santiago soil gravel and a water table located below 50 m depth (Ortigosa & Retamal, 1994).

Although there are studies that have analyzed the behavior of discontinuous anchored pile supports based on in situ measurements, most of these are static analyses since these structures lack monitoring instrumentation to measure their seismic response. Therefore, numerical modeling is a crucial tool for analyzing this dynamic behavior, especially considering that dynamic analysis is very important in Chile, a seismically active country where this constructive method is widely used. This research examines the dynamic response of a group of discontinuous anchored piles in a representative excavation.

The study uses PLAXIS 3D to model a real excavation with parameters experimentally calibrated by Salas (2017). To use the calibrated parameters most reliably, the same case study has been employed in this work, preserving the identical physical characteristics of the excavation and the soil stratification as modeled by Salas (2017). The 3D excavation model includes two configurations of 13 and 48 piles, respectively, including a corner pile. Both static and dynamic behaviors are evaluated through this numerical model, comparing the behavior of the corner pile with the rest of the piles.

For the dynamic analyses, bidirectional inputs are considered, specifically using a Ricker wavelet with the same frequency as the soil, a second wavelet with the frequency corresponding to the pile length, and the Mw 8.8 earthquake that struck Maule, Chile, in February 2010, recorded at the Rapel rock station.

The primary objective of this research is to understand the dynamic 3D behavior of excavations supported by discontinuous anchored piles under bidirectional seismic loading. Additionally, this study compares the results to evaluate the conservativeness of the relevant standards for such geotechnical structures.

2 Objectives

2.1 General Objective

The main objective of this research is to understand the dynamic 3D behavior of excavations supported by discontinuous anchored piles under bidirectional seismic loading. Additionally, this study compares the results to evaluate the conservativeness of the relevant standards for such geotechnical structures.

2.2 Specific Objectives

1. Use the FE software PLAXIS 3D to 3D model a pile-supported excavation in Santiago gravel soil.
2. Analyze the soil pressure, deformation, and internal forces induced on the excavation piles under bidirectional Ricker Wavelet loading.
3. Analyze the soil pressure, deformation, and internal forces induced on the excavation piles under bidirectional seismic loading (Rapel's 85 station record).
4. Conduct a comparative analysis between the results obtained from Ricker Wavelet and seismic loading simulations.
5. Compare and contrast the model outcomes with calculations derived from the Mononobe-Okabe (MO) method and the Chilean standard NCh433 Of. 2009.

3 Methodology

The methodology to achieve the proposed objectives of this research is described below.

- Before starting numerical modeling, a literature review was conducted to understand the state of the art, and the standards governing these structures, and focus the direction of this research. The result of this review indicated a lack of sufficient knowledge about the 3D dynamic behavior of retaining walls.
- This research uses the work of Salas (2017) as a reference, where parallel gradation was used to define and conduct tests and to model a 3D section of two half-piles of a real excavation in Santiago, for which inclinometer measurements are available. For more information refer to chapter 4.3.
- The HS-Small parameters derived from Salas (2017), the real excavation, and its inclinometer measurements were used as the basis for generating the 3D excavation model.
- During the static analyses, it was observed that the anchor tension derived from the design and construction of the excavation did not reproduce the deformation measured with the in-situ inclinometer. Therefore, after an exhaustive review, it was decided to prioritize reproducing the deformation over the anchor tension, using a lower pre-tension.
- Once the static analyses were satisfactorily completed, achieving a displacement that adequately reproduced the inclinometer measurements, two dynamic runs were performed: one with a bidirectional Ricker wavelet with a frequency equal to the soil frequency, and the other with a bidirectional Ricker wavelet with a frequency equal to the pile frequency.
- After completing the dynamic analyses with the Ricker wavelet inputs, a seismic run was generated. This model could not be performed with the initial configuration, so the configuration was quadrupled to ensure no pile was located at the model's boundary. Consequently, a static analysis of both configurations was redone to determine if their dynamic results could be compared, yielding practically identical responses.
- The seismic run, having a configuration four times larger than the Ricker runs, required significantly more computation time. Therefore, information from strategic points, i.e. a fraction of the 48 modeled piles, was saved.
- After completing the dynamic analysis of the seismic run and comparing it with the Ricker runs, the results were compared with those calculated using Mononobe-Okabe and the Chilean standard NCh433, which proposes an equation for induced dynamic pressure.

4 Literature Review

4.1 Discontinuous Piles as a Soil Retaining System

The discontinuous anchored pile support system is a construction technique commonly used for the stabilization and support of excavation walls, trenches, and other subterranean structures. It relies on installing spaced piles, anchored with steel bars or cables, to resist lateral soil pressure and prevent the collapse of excavation walls. These anchors are tensioned to stabilize the wall by transferring forces to more stable soil layers.

In Santiago de Chile, the increase in population density has resulted in a growing trend towards high-rise construction adjacent to existing buildings. This proximity requires stable excavation methods that protect both the excavation and neighboring structures. As a result, the discontinuous pile support system has gained popularity for its effectiveness in deep excavations. Additionally, due to the seismic activity in the region, seismic verification of these systems is mandatory.

The region's geological conditions, characterized by Santiago gravel—a dense material with favorable mechanical properties and a deep water table (approximately 50 meters depth)—make it an ideal choice for implementing this construction method (Ortigosa & Retamal, 1994). This combination of cost-effectiveness, ease of installation, and favorable soil properties has driven its extensive application across Santiago.

A prominent example of this technique is the Parque Oriente building, where a 21.2m deep excavation was supported by discontinuous anchored piles. Salas (2017) conducted a detailed study of this case, comparing in situ measurements with numerical models, demonstrating the efficiency of the system under both static and dynamic loads. The research highlighted how the arching effect—the redistribution of stresses between piles—helps reduce soil pressures acting on the retaining system. Figure 1 illustrates the case study excavation and anchor characteristics.

Rozic (2012) further studied this phenomenon in a deep excavation located at the Beauchef Poniente Building. This case involved piles anchored at multiple levels, modeled using FLAC 2D, showing that the corner piles experienced higher stresses due to the three-dimensional behavior of the soil-pile interaction. The results underscored the importance of considering corner effects in deep excavations, where the lateral soil pressure distribution is non-uniform.

Figure 2 below illustrates a typical discontinuous anchored pile support system in Santiago gravel, demonstrating how the piles and anchors interact with the soil to maintain stability. Figure 3 shows another example in Santiago, Chile.

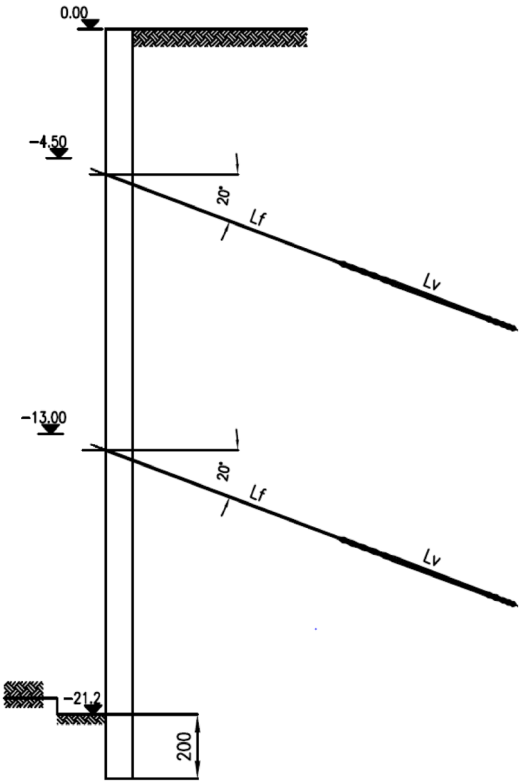

Figure 1 Case study cross section. (F. Salas, 2017)

Figure 2 Discontinuous anchored pile support system on Santiago gravel example (Sáez & Ledezma, 2010).

Figure 3 Anchored piles from the excavation of Los Trapenses Mall, Terratest.

The main advantages of using discontinuous anchored piles include:

1. **Cost-effectiveness:** Compared to continuous walls, discontinuous piles require fewer materials and incur lower installation costs.
2. **Adaptability to Santiago gravel:** The dense, well-drained nature of the gravel reduces the risk of excessive deformation or water infiltration during excavation.
3. **Seismic resistance:** The design methodology has proven to be resilient during the earthquakes that Santiago has experienced. However, due to the limited information available regarding the dynamic behavior of these structures, their seismic resistance may be attributed to the conservative design approach.

However, limitations include the need for detailed numerical analysis to account for complex behaviors such as the arching effect, as well as the three-dimensional interactions, particularly in corners and irregular excavation geometries.

In conclusion, the discontinuous anchored pile support system has proven to be an effective solution for deep excavations in Santiago de Chile. Its adaptability to the region's favorable soil conditions and its cost-efficiency make it a preferred choice in many construction projects. However, considering the seismic risks in the region, it is crucial to incorporate advanced 3D numerical models to ensure the safety and stability of these systems, particularly in the design of corner piles and during seismic events.

4.1.1 Design Methodology in Santiago Gravel

This chapter examines the design of retaining systems in gravel soils in Santiago, Chile, within the framework of international standards and recommendations. It focuses on how Chilean regulations have adapted methodologies from German, European, and American standards to create robust and effective practices. These adaptations ensure that the design principles and construction techniques meet the unique demands of local soils, seismic activity, and construction practices.

The typical construction method for discontinuous retaining systems involves anchored reinforced concrete piles. Depending on the soil conditions—such as gravel, sandy, or soft soils—the piles may either be excavated manually and concreted in situ or mechanically driven. For these piles, common concrete grades such as G20 or G25 are used, and the reinforcement steel typically follows the A630-420H specification. The number of anchor lines, used to stabilize the system, varies depending on the excavation depth.

Building on established international guidelines, Vásquez (2018) points out that the design principles applied to retaining systems in Santiago are based on standards from Germany, Europe, and the United States, which have proven effective in local applications. Table 1 summarizes the key standards and recommendations that inform the design process.

Table 1 Standards used as the basis of design.

DIN Standard	DIN 1054:2010-12 Subsoil - Verification of the safety of earthworks and foundations
	DIN 4084:2009-01 Soil - Calculation of embankment failure and overall stability of retaining structures
	DIN 4125 - Ground anchorages – Design, construction, and testing
	DIN EN 1537:2014-07 Execution of special geotechnical works - Ground anchors; German version EN 1537:2013
Design recommendations	EAB, “Recommendations on Excavations,” 2nd Ed., German Geotechnical Society, DGGT, 2008.
	EAU 2012, “Recommendations of the Committee for Waterfront Structures Harbours and Waterways”.
	Geotechnical Engineering Handbook, Volume 3: Elements and Structures; Ernst and Sohn (A Wiley Company); Berlin, 2003
U.S. Standard	ACI 318-08: Código de diseño de Hormigón Armado
	ANSI/AISC 360-10. American Institute of Steel Construction (AISC)
Chilean Standard	NCh 3206.Of2010 “Geotecnia – Excavaciones, entibaciones y socalzados – Requisitos”, Norma Chilena Oficial, Instituto Nacional de Normalización.
	NCh 433 Of. 1996 Mod. 2009 + DS 61/2011 “Diseño Sísmico de Edificios”, Norma Chilena Oficial, Instituto Nacional de Normalización.

To implement these design principles, engineers typically rely on two-dimensional structural modeling software, such as GGU-Retain. This software simulates the interaction between the piles and soil by

incorporating geometric and stiffness properties. It uses force equilibrium methods to calculate internal forces within the piles and the loads on each anchor line, adhering to German publications like the "Recommendations of the Working Group for Excavations (EAB)" and the "Committee for Port Structures (EAU 2004)." These standards define soil pressure distributions and allow for the integration of either the old or new DIN 1054 standard or even customized pressure distribution, depending on the specific project requirements.

In terms of geotechnical prerequisites, the design of retaining systems begins with essential soil studies. These include SPT tests, test pits, laboratory strength tests (such as direct shear or triaxial tests), and determining the water table level. These studies help to establish the soil characteristics needed for proper design, particularly in assessing the pressures acting on the structure.

For static and seismic load conditions, the design must account for a combination of active, passive, and at-rest soil pressures. These forces ensure that the retaining structure's embedment length is sufficient and that the required safety factors are met. The redistribution of soil pressures is typically based on DIN 4085 and EAB 2006 standards, although local Chilean standards, such as NCh 3206, often simplify these distributions by adopting a rectangular pressure model. This approach, while straightforward, is effective for the discontinuous anchored pile systems commonly used in Santiago.

Seismic considerations play a critical role in the design, especially given Chile's seismic activity. The Chilean standard NCh433 Of. 2009 indicates that for underground walls, the lateral pressure induced by earthquakes is a uniformly distributed, pseudo-static load calculated using the following equation:

$$\sigma_s = 0.3\, C_R\, \gamma\, h_m \frac{A_0}{g} \tag{1}$$

Where,
C_R: Coefficient equal to 0.45 for dense soils and 0.7 for loose or soft soils. In this case 0.45.
γ: Wet unit weight of the soil or fill deposited contiguous to the basement walls
h_m: Wall height in contact with the soil
A_0: Effective acceleration according to the standard, 0.3 correspond to Santiago, Chile.

From this expression, the internal forces resulting from this pseudo-static load can also be calculated. These forces will be used in this study to compare the results obtained through the dynamic numerical model and their proximity to the maximum obtained according to the Chilean standard.

The seismic coefficients, as defined by NCh 3206 Of. 2010, are calculated based on the effective acceleration of the seismic zone and the structural constraints of nearby buildings. The lateral pressures caused by earthquakes are evaluated using limit equilibrium methods, applying both horizontal and vertical seismic coefficients.

When designing for additional loads, the imposed live loads are dictated by the same Chilean standard, which specifies a minimum vertical live load of 12 kN/m². For buildings with multiple floors or adjacent underground parking structures, an additional minimum live load of 11 kN/m² is included. In seismic scenarios, the base shear effect is incorporated into the load distribution, adjusting the design accordingly.

The safety of the retaining systems is ensured through various safety factors. These include factors for passive soil resistance (both static and seismic), reinforced concrete (following ACI-318), structural steel (per ANSI/AISC 360-10), and post-tensioned anchors. Additional safety factors are applied to anchor lengths to account for free length calculations.

The spacing between piles is another critical factor in the design. In Santiago's gravel soils, the recommended spacing is typically no more than 3.5 meters between pile axes. However, this may be adjusted based on the moment diagrams obtained during analysis, and additional anchor lines may be considered if necessary. To maintain the soil's integrity between piles, shotcrete is commonly used to prevent moisture loss and preserve apparent cohesion.

Anchor design also plays a crucial role in stabilizing the retaining system. Engineers must carefully consider the anchor material, free length, and bulb length to ensure proper lateral support. The placement angle of the anchors should not exceed 30° relative to the horizontal, with compensatory measures taken if it does. The design of anchor bulbs is based on friction values from design tables, with the final length determined using the Ranke-Ostermayer method. This method ensures that the anchor length provides sufficient stability, considering the most critical failure scenarios.

Finally, displacement control is essential in deep excavations supported by discontinuous anchored piles. For projects where excavation depth meets or exceeds the monitoring requirements set by NCh 3206, the system's deformation must be carefully monitored using inclinometers. This is especially important for projects near sensitive structures, such as monuments, where allowable deformations are tightly controlled.

4.2 Numerical Analysis

In deep excavation projects, pile-supported retaining systems are widely used to provide lateral support in soils with complex behavior. These systems rely on the interaction between the piles, anchors, and surrounding soil to ensure stability under various load conditions, including static, dynamic, and seismic forces.

The effectiveness of these retaining structures, particularly in discontinuous pile systems, is largely influenced by a phenomenon known as the arching effect, where stresses within the soil redistribute from yielding regions to more stable areas. This redistribution is critical in optimizing the load-bearing capacity and ensuring the safety of excavations, especially in projects involving deep and complex soil conditions like those found in Santiago's gravel.

Before diving into the specifics of numerical analysis, it is essential to first review the current state of the art regarding pile-supported excavation methods and the arching effect. This includes an overview of both experimental and numerical research that has provided valuable insights into the mechanics of soil-pile interaction and the nonlinear behavior of lateral soil pressures. Figure 4 provides a visual representation of the rotation of principal stresses in the soil adjacent to the piles, as observed in studies by Chen & Martin (2002), which will help to contextualize the upcoming discussions.

4.2.1 Arching Effect Numerical Analysis

Discontinuous pile structures are governed mainly by the arching effect which consists of the redistribution of stresses, from the yielding parts to less-yielding/restrained parts of the soil. Chen & Martin (2002) in their study on soil-structure interaction for soil stabilization systems, induced the soil displacement around two concrete elements, allowing us to observe changes in the direction of principal stresses, illustrating this effect's geometric configuration in Figure 4.

This phenomenon has been demonstrated by experimental and numerical studies (e.g., Harrop-Williams, 1989, Khatami et al., 2019, Medina Díaz, 2002, Pardo, 2013). On the other hand, for lateral support structures, research has focused on studying the nonlinear distribution of lateral soil pressure on structures (e.g. Paik & Salgado, 2003, Zhu et al., 2013).

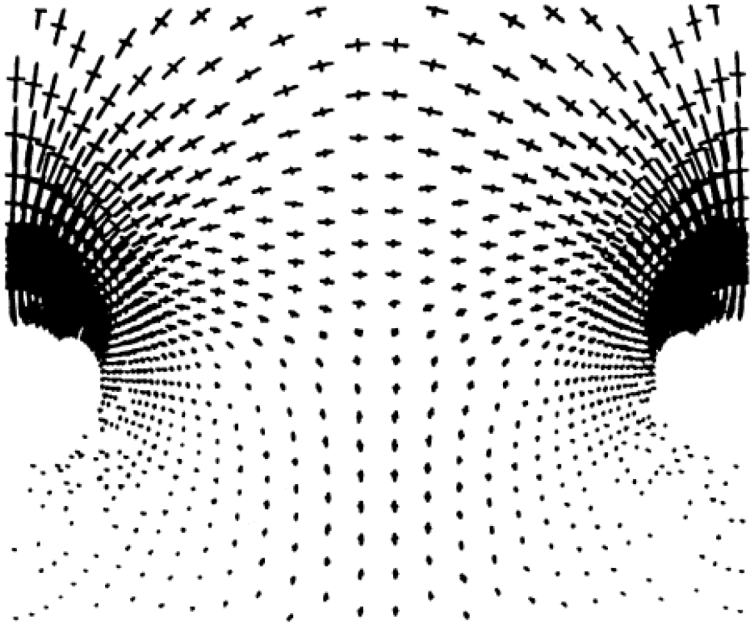

Figure 4 Diagram of the rotation of principal stresses in the soil adjacent to the piles. (Chen & Martin, 2002)

4.2.2 Discontinuous Anchored Pile Support System Numerical Analysis

Most 2D numerical models of discontinuous anchored pile support have focused on static deformations, in such a way that they can replicate the real lateral strains developed throughout the different construction stages. For example, Boldrini & López (2014) numerically modeled a retaining system consisting of anchored piles for deep excavation in the Santiago gravel and compared the results with actual in-situ measurements. They reported a good concordance between both results. Similarly, López & Sanhueza (2019) developed a study of an excavation supported by anchored piles. They reported changes in the pressure distribution as the construction stages progressed, obtaining conservative designs. In the same way, Rozic (2012) modeled a real excavation in Gravel soil with instrumented 28.5 m piles anchored on three levels using FLAC 2D (Beauchef Poniente Building). The three studies compared the modeled lateral deformation with the in situ measured lateral deformation and achieved accurate results. Similarly, Raddatz & Taiba (2017) compared the in-situ measurements with the numerical models of the lateral deformation obtained with three different software; PLAXIS 2D, GGU-Retain and CYPE, obtaining that PLAXIS 2D provided the curve that best fits the results measured at the site for the last construction stage while CYPE shows low displacement in the first half of the pile and GGU-Retain, when considering a uniform distribution of the pressure, obtained higher loads in the area closest to pile's head.

However, while 2D models have provided valuable insights into lateral deformation during construction stages, they are limited in their ability to capture the full three-dimensional behavior of the system. To address these limitations, 3D numerical models have proven more effective in representing the complex interactions in deep excavations supported by anchored piles. For example, Zhu et al. (2013) statically modeled the corner of a deep excavation supported by anchored piles, highlighting how the corner effect restricts deformation and alters the internal forces on the piles and surrounding soil. This behavior is particularly significant in corner piles, where conventional 2D models may underestimate the stresses involved. Vásquez (2018) further explored this by examining concave corners, concluding that such configurations improve the performance of retaining systems by maintaining manageable deformation levels and safety factors similar to side walls without 3D boundary effects.

Nevertheless, despite the various investigations developed for this retaining system, its dynamic response to seismic events is still unknown since the design of these structures is not usually implemented with a seismic response measurement system. For this reason, numerical models have

become a valuable tool for studying the development of stresses and strains in these excavations. Sáez & Ledezma (2010) and Sáez & Ledezma (2012) concluded that the Chilean code (NCh433 standard) underestimates the seismic bending moment response in the upper part of the piles and is over-conservative for the lower part, specifically for the studied cases, which consisted of a 3D vertical 'slice' including two adjacent half-piles and the soil in between.

Similarly, Salas et al. (2019) modeled a 2D excavation and used as input motion two great seismic Chilean events (Mw8.8 Maule earthquake and the Mw8.0 Valparaíso earthquake). Results showed a maximum seismic moment 157% greater than the maximum static value, both obtained from the modeled excavation, and the maximum seismic moment is also 20% lower than the maximum design moment calculated using the limit equilibrium methodology, the current design procedure, refer to chapter 4.1.1.

While their 3D slice model offered important insights into pile behavior, its limited scope did not fully account for the three-dimensional interactions seen in broader excavations. Particularly, the corner effects and interactions between piles were not addressed, which are critical factors in real-world conditions. This limitation underscores the need for larger, more comprehensive 3D models like the ones presented in this study, which analyzes 13 and 48 piles in various configurations.

The parameters calibrated by Salas et al 2019 to represent Grava de Santiago were used in this study. Complementary to this study, Aravena (2020) evaluated a 3D three-pile excavation, he obtained that the lateral seismic pressure is lower than those obtained from the limit equilibrium analysis. Therefore, to achieve a correct characterization of the discontinuous anchored pile support behavior throughout all its depth, it is extremely important to take into account a complete 3D computational study.

Considering the limitations of both 2D and simplified 3D models, this research aims to provide a more complete analysis by evaluating the static and dynamic response of a deep excavation supported by discontinuous anchored piles in Santiago gravel. Using PLAXIS 3D, this study explores the excavation's behavior under various seismic conditions, including different Ricker wavelets and a seismic signal, applied in two directions, allowing for a thorough investigation of the system's performance throughout all phases of loading.

4.3 Monitoring and Dynamic Analysis of a Discontinuous Pile-Supported Deep Excavation in Santiago Gravel

When conducting numerical modeling of soils, it is essential to select and calibrate a constitutive model that accurately replicates both the static and dynamic behavior of the material. The parameters and the Hardening Soil Small Strain constitutive model used in this modeling are based on the research by Salas (2017), which includes static and dynamic analyses with experimentally calibrated parameters.

Salas performed an experimental characterization of Santiago Gravel soil using scaled samples and the parallel gradation method proposed by Mariachi et al. (1972)(Mariachi et al., 1972). Subsequently, earthquake simulations were conducted using PLAXIS 2D and 3D for a deep excavation of Parque Oriente building supported by anchored piles in Santiago gravel which counts with available in situ deformation measurements. It's worth noting that the 3D model considered only the width between two half piles. This work allows us to replicate the deformations and static stresses observed in the case study, with the expectation that its parameter calibrations can be applied to a larger 3D excavation model.

To achieve the experimental characterization of Santiago Gravel, the author opted for the parallel grading method to downsize particles for common tests on a smaller scale. This method was selected for its realism, preserving the particle size sequence of the original sample, in contrast to scalping/truncated grading or replacement techniques. It is essential not to exceed 10% fines content, maintaining consistent particle mineralogy, particle shape, and sample aspect ratio.

The scaling process was validated through a series of in situ triaxial tests on 1 m diameter Grava de Santiago, as conducted by Kort (1979). Representative samples for applying the parallel grading method were extracted at a depth of 10 m. Table 2 illustrates the comparison between the properties of the scaled sample and the soil prototype studied by Kort (1979).

Table 2 Properties of the sample used for scaling and the soil prototype (Kort et al., 1979).

Material	**Fines Content (%)**	$C_u = \frac{D_{60}}{D_{10}}$ **(-)**	$C_c = \frac{{D_{30}}^2}{D_{10} \times D_{60}}$ **(-)**	ρ_{max} **kN/m^3**	ρ_{min} **kN/m^3**
Kort (1979)	2.0	77.8	5.20	23.8	19.7
Scaled material	9.0	70.5	5.24	23.5	19.3

Kort (1979) conducted large-scale Consolidated Monotonic Drained Triaxial (CID) tests in situ under four confinement levels: 220, 440, 600, and 830 kPa. These results were used to compare the stress-strain trajectories obtained from scaled sample tests at corresponding confinement levels and relative density. Figure 5 displays the results of the CID triaxial test, reference curves from Kort (1979), and simulations using the HS-Small model (Benz, 2007) available in PLAXIS software.

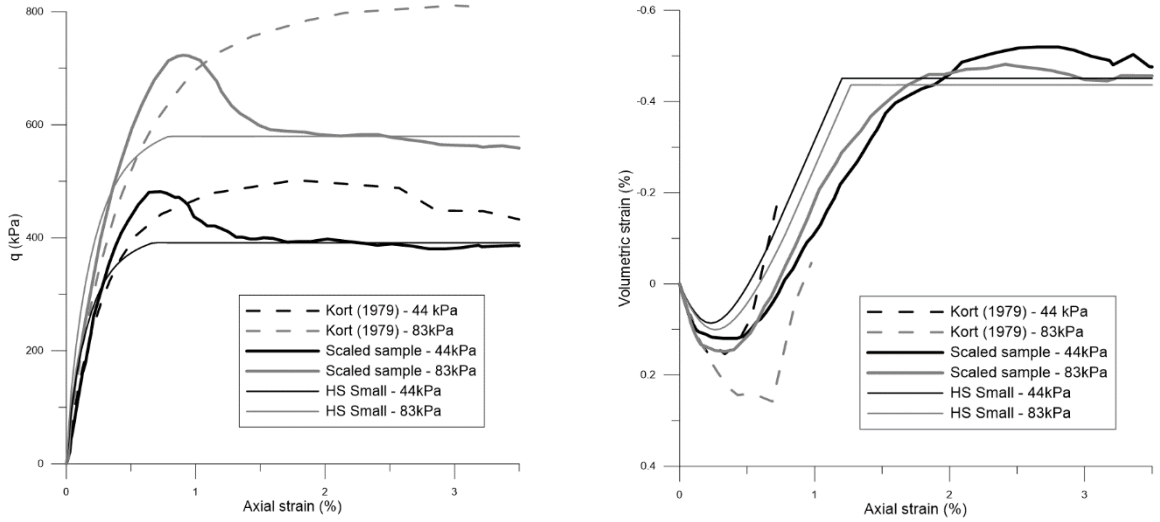

(a) (b)

Figure 5 Comparison between references curves (Kort, 1979), CID triaxial test in scaled samples and simulation paths according to HS-Small. (a) deviatoric stress versus axial strain and (b) volumetric strain versus axial strain. (Salas, 2017)

By complementing these results with a geophysical survey to adjust low-strain parameters, an advanced constitutive model was calibrated. In broad terms, the characterization research results demonstrated a strong alignment with the mathematical formulation of the HS-Small model. This constitutive model is based on the usual Hardening Soil (isotropic hardening), but two more parameters are included that allow modeling the range of shear deformation in which the soil behaves linearly.

In the Appendix, a brief description of the constitutive model is presented, based on the PLAXIS 3D Manual and the research by Salas (2017).

To use the calibrated parameters in the most reliable manner, the same case study has been employed in this work, preserving the identical physical characteristics of the excavation and the soil stratification as modeled by Salas (2017).

5 Case Study

The case study in this report is the deep pile-supported excavation used for Salas (2017), located in the Las Condes district of Santiago. The excavation was 21.2m deep and is retained with temporary discontinuous bored cased piles, laterally braced with two lines of ground anchors.

Unlike the model proposed by Salas (2017), which represented a 3D section of the excavation supported by only 2 half-piles, the current study addresses two configurations of broader excavation with a total of 13 piles and 48 piles; and one of these piles is located in the corner of the excavation.

In summary, this work complements the previous research of Salas (2017) by not only dynamically analyzing a larger model, but also assessing whether the calibration performed is compatible with 3D models by comparing it with the deformation measured by the inclinometer in the static analysis. Furthermore, it is important to point out that the behavior of this construction method is dominated by the three-dimensional arch effect.

The case study in this report focuses on the deep pile-supported excavation analyzed by Salas (2017), located in the Las Condes district of Santiago. The excavation was 21.2m deep and was retained using temporary discontinuous bored cased piles, laterally braced with two lines of ground anchors.

Unlike the model proposed by Salas (2017), which represented a 3D section of the excavation supported by only two half-piles, the current study examines two broader excavation configurations: one with 13 piles and another with 48 piles, with piles located at the corner of the excavation.

In summary, this work complements the previous research of Salas (2017) by not only dynamically analyzing a larger model, but also assessing whether the performed calibration is compatible with 3D models by comparing it to the deformation measured by the inclinometer in the static analysis. Furthermore, it is important to highlight that the behavior of this construction method is governed by the three-dimensional arch effect.

For a better understanding between both studies, Figure 6 shows 3 models: the one used by c and the two used in this study.

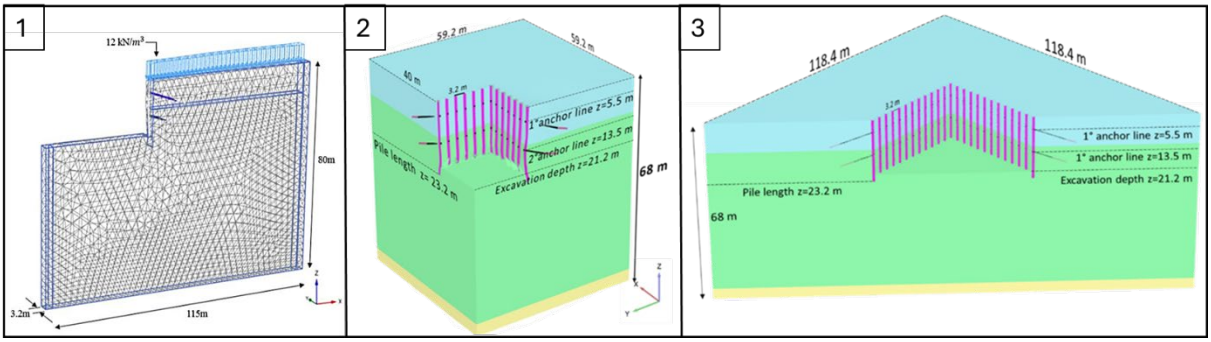

Figure 6 Models used by Salas (2017) and by this research. (1) Salas's model (2) Model Configuration 1 (3) Model Configuration 2.

5.1 Numerical Model Description

Two excavation configurations were considered for the numerical models which are described below.

5.1.1 Model Configuration 1

The first excavation configuration of the numerical model consists of 19.2 m x 19.2 m x 21.2 m, length, width and depth, respectively, which corresponds to a representative fraction of a larger excavation in the Santiago gravel soil. The system is supported by 13 bored piles in L arrangement, i.e., 2 consecutive faces of the excavation are supported by 6 piles each and share 1 corner pile. This configuration was chosen to be able to study the corner effect in static and dynamic analysis. In order to reduce the time of computations, a representative fraction of a larger excavation is used. The model considers two scenarios, where it analyzes the dynamic behavior due to two different 2-D Ricker wavelett. For a better interpretation of results, piles parallel to the y axis are designated as Group 1 and piles parallel to the x axis are designated as Group 2. For more details on the pilot-anchor configuration, see Figure 42 in the Appendix.

The soil cube where the excavation is modeled, is composed of a square dimension of 59.2m per side, plan view, and a depth of 68m. The model depth was selected to achieve shear wave velocities corresponding to rock and the plan extension was chosen to prevent the active wedge of the excavation from reaching the model boundary; a 15-meter clearance was added to accommodate any changes that may occur during the dynamic phase.

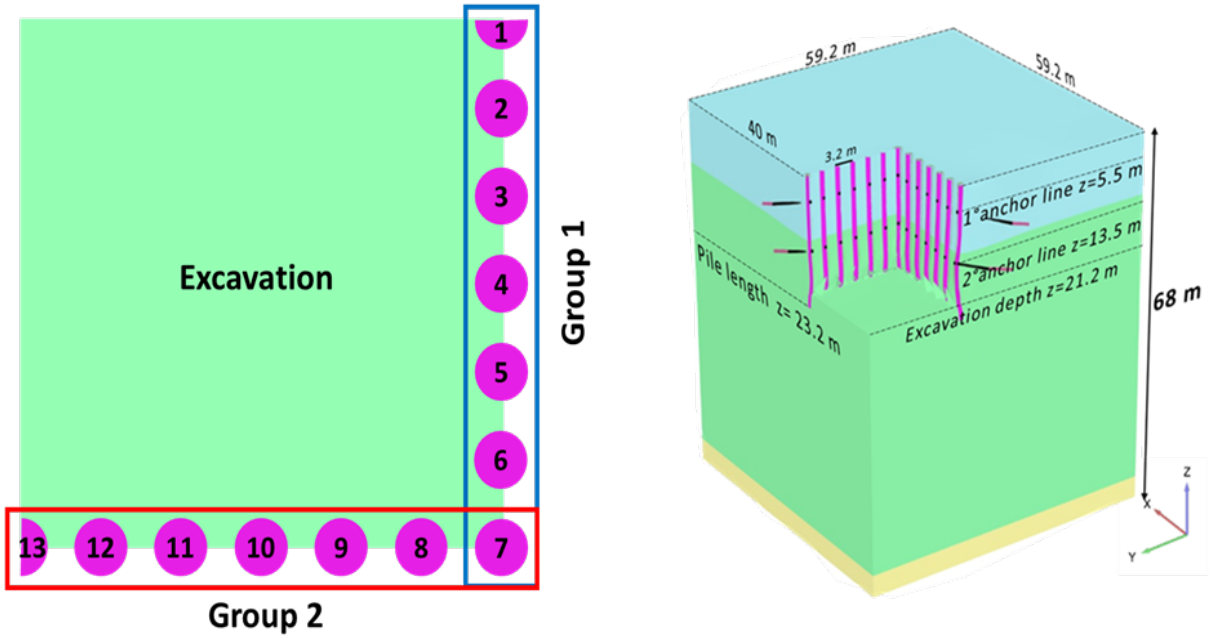

Figure 7 Excavation model and pile aggrupation. Configuration 1.

5.1.2 Model Configuration 2

Due to the inability of the first configuration to run a seismic input presumably because of the border conditions which coinciding with two half piles and the higher seismic motion requirement, it was required to quadruplicate the excavation model, resulting in a complete excavation model, with no pile adjacent to the border. It maintained the soil and excavation characteristics of the first configuration, the only difference in the second one is that there is no half pile nor border pile.

The second excavation configuration of the numerical model consists of 38.4 m x 38.4 m x 21.2 m, length, width and depth, respectively, which corresponds to an excavation in the Santiago gravel soil. The system is supported by 48 bored piles. The model considers one scenario, where it analyzes the dynamic behavior due to a 2-D seismic input. For a better interpretation of results, piles parallel to the *y* axis are designated as Group 1 and piles parallel to the x axis are designated as Group 2. It is important to note that, due to the large number of piles modeled in this configuration, it was decided that only 13 out of the 48 piles will be analyzed in this study, located on the excavation half where the axis of seismic input symmetry lies.

The soil cube where the excavation is modeled is composed of a square dimension of 118.4 m per side, a plan view, and a depth of 68 m. As in the model configuration 1, the model configuration 2 depth was selected to achieve shear wave velocities corresponding to rock and the plan extension was chosen to prevent the active wedge of the excavation from reaching the model boundary; a 15-meter clearance was added to accommodate any changes that may occur during the dynamic phase.

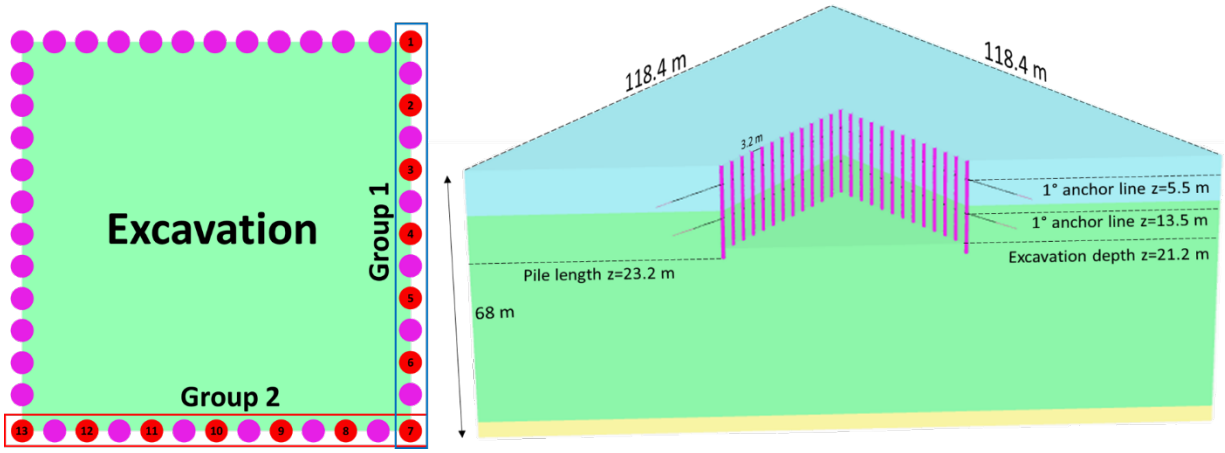

Figure 8 Pile arrangement and Diagonal cut of the excavation model. Configuration 2.

5.1.3 Soil and Construction Description

The numerical models only differ in size, i.e., the second model corresponds to the first model quadruplicated, so they share the characteristics of all the materials that compose them (pile, soil, anchor, etc.) and have the same construction stages.

The modeled soil is composed of the 2nd Deposit of the Mapocho River in its first 11.3 m of depth, then follows the 1st Deposit up to 64 m depth and ends with 4 m of a hypothetical bedrock (Figure 8). Although the bedrock at this point in Santiago is deeper, given the confinement of the model at this depth, elastic behavior can be assumed with properties corresponding to a deep gravel or soft rock (see Table 8). The plan extension is chosen to avoid the active wedge of the excavation reaching the model boundary, and a 15 m minimal clearance is added, to account for the changes that may occur in the dynamic phase. On the other hand, at the ground level, a uniform overload surface of 12 kN/m^2 extends on the soil around the excavation, which represents the load added by a neighboring street.

Table 3 Geotechnical parameters for Santiago gravel.

Material	Depth (m)	Unit weigh γ (kN/m^3)	Internal friction angle, ϕ	Cohesion (kPa)
Second Deposition	11.3	22	45°	15
First Deposition	64	22.5	45°	25

The piles are 0.88 m in diameter and 23.2 m long, with a 3.2 m center spacing and 2 anchor lines. Soil volume elements governed by a Linear Elastic behavior were used to model the piles and an interface was created in their shaft to evaluate the pressure exerted by the soil on the pile. Furthermore, because of modeling a representative fraction of a larger excavation, the 2 piles in the model boundary are represented by a half pile, that is a -cylinder divided longitudinally in half. For this reason, the two anchor lines corresponding to these piles are prestressed with half the load.

Table 4 Pile's mechanical parameters.

Parameter	Description	Units	Pile
γ	Unit weight	kN/m^3	24
E^{ref}	Secant stiffness in standard drained triaxial test	kPa	25,000,000
E_{oed}	Tangent stiffness for primary oedometer loading	kPa	27,780,000
G^{ref}	Reference shear modulus for p'_{ref} at very smalls strains ($\varepsilon < 10^{-6}$)	kPa	10,420,000
$e_{initial}$	Initial void ratio	-	0.50

The 2 anchor lines are installed, for each pile, at a depth of 4.5 m and 13 m, where their free length is modeled by a "node to node" element while a rigid connection embedded beam was used for the bulb. The load used to prestress the pile's anchors are shown in Table 5 and the mechanical properties are in Table 7. The prestress load in the anchors was chosen from iterations in the static phase of the model, in such a way that the final static displacement of the piles coincided with the final displacement measured with an inclinometer in the excavation of the Parque Oriente building Salas (2017).

Table 5 Anchor lines prestress.

Anchor line	Depth (m)	Piles prestress (kN)	Border piles prestress (kN)
First	4.5	440	220
Second	13	535	267.5

Table 6 Anchor lines mechanical properties.

Anchor line	EA (kN)	Axial skin resistance (kN/m)	Base resistance (kN)
Anchor	11,0000	-	-
Embedded beam	244,463	400	1,000,000

The static phase is divided into 8 subphases that simulate the construction sequence of a pile-supported excavation. These stages are detailed in Table 7. For more details on the constructive stages, see Figure 34 to Figure 41 in the Appendix.

Table 7 Excavation constructive stages.

Stage	Excavation depth (m)	Stage Description
1	z = 0.0	Initial phase
2	z = 0.0	Application of the surcharge load (12 kPa)
3	z = 0.0	Installation of the pile
4	z = -5.5	First excavation
5	z = -5.5	Installation and pre-stressing of the first anchor line
6	z = -13.5	Second excavation
7	z = -13.5	Installation and pre-stressing of the second anchor line
8	z = -21.2	Excavation until the foundation seal level

The 3D model uses tetrahedral elements of 10 nodes. This mesh was defined as "very coarse" and has been locally refined in key places such as anchors, piles, and soil around the excavation. It is formed of elements whose average size is 1.978 m and 1.630 m for Configuration 1 and 2, respectively, which guarantees at least 8 elements per wavelength, considering the most restrictive Ricker wavelet frequency as the cut-off frequency. On the other hand, to minimize the wave reflection on the lateral edges in the dynamic phase, the free field condition is used in the input direction (i.e., in a single direction in the case of the one-dimensional Ricker wave and in two directions in the case of the two-dimensional Ricker wave). This condition imposes free field motion to the sides and absorbs the reflected secondary waves. To ensure that the waves reflected by the upper layers are absorbed by the base, the compliant base condition is used at the bottom of the model (PLAXIS 3D Manual).

5.1.4 Inclinometer

The reference excavation was monitored, and one of the piles, located far from the corner, was instrumented with an inclinometer casing attached to the reinforcement cage. The inclinometer measurement from the final stage of construction will be used to evaluate the deformation obtained from the numerical model in the static analysis, similar to the approach used by Salas (2017).

5.2 Soil Constitutive Model and Parameters Calibration

As mentioned before, to reproduce the static behavior of the material, the parameters and constitutive model used in this modeling are chosen based on the research by Salas (2017). Therefore, the constitutive model Hardening Soil: Small Strain (Benz, 2007) is used to model Santiago gravel, its geotechnical parameters are presented in Table 8. Also, the Linear Elastic constitutive model is used for Bedrock, and the parameters are shown in Table 9.

Table 8 Santiago gravel HS-Small parameters calibrated by Salas (2017).

Parameter	Description	Units	First Deposition	Second Deposition
m	Power for the stress-level dependency of stiffness	-	0.51	0.55
E_{50}^{ref}	Secant stiffness in standard drained triaxial test	kPa	275,000	80,000
E_{oed}^{ref}	Tangent stiffness for primary oedometer loading	kPa	190,000	130,000
E_{ur}^{ref}	Unloading/reloading stiffness from frained triaxial test	kPa	900,000	350,000
G_0^{ref}	Reference shear modulus for p'_{ref} at very smalls strains ($\varepsilon < 10^{-6}$)	kPa	750,000	400,000

Parameter	Description	Units	First Deposition	Second Deposition
$\gamma_{0.7}$	Threshold shear strain at which $G_s = 0.7G_0$	-	0.0011	0.0008
c'	Effective cohesion	kPa	35	15
φ'	Effective angle of internal friction	°	45	45
ψ	Angle of dilatancy	°	15	10
σ_t	Tension cut-off and tensile strength	kPa	-	-
ν_{ur}	Poisson's ratio for unloading/reloading	-	0.2	0.3
R_f	Failure ratio $\frac{q}{q_a}$(Default $R_f = 0.9$)	-	0.9	0.9
K_0^{nc}	K_0 −value for normal consolidation	-	0.43	0.65
$e_{initial}$	Initial void ratio	-	0.150	0.150
e_{max}	Maximum void ratio	-	0.154	0.154

Salas (2017) highlights the limitations of the HS-Small model, particularly in its inability to reproduce the peak stress typically observed in dense soils. This limitation is attributed to the hyperbolic nonlinear stress-strain relationship of the model. However, Salas suggests that this shortcoming is unlikely to significantly affect the results, as the maximum expected axial strain does not exceed 0.5%. Moreover, the model adequately captures the transition between contractive and dilative behavior at low strains.

In the case of the Bedrock, the Linear Elastic constitutive model was selected, the parameters are shown in Table 9.

Table 9 Bedrock parameters, Salas (2017).

Parameter	Description	Units	First Deposition
E^{ref}	Secant stiffness in standard drained triaxial test	kPa	7,800,000
E_{oed}	Tangent stiffness for primary oedometer loading	kPa	10,500,000
G^{ref}	Reference shear modulus for p'_{ref} at very smalls strains ($\varepsilon < 10^{-6}$)	kPa	3,000,000
$e_{initial}$	Initial void ratio	-	0.50

5.3 Input Motion

5.3.1 Ricker Wavelet Description

To reduce the computing time, it was decided to use Ricker Wavelets. This synthetic signal has been widely used as an alternative to seismic data, as its asymmetrical amplitude spectrum can represent the attenuation feature of seismic wave propagation through viscoelastic homogeneous media. In this research, two different Ricker wavelets are used (Figure 9). The Wavelet main frequencies used are 3.04 Hz and 6.46 Hz, which are the soil natural frequency and the pile natural frequency, respectively. Henceforth in this document, these wavelets will be referred to as RW-S and RW-P. For the 2D analysis, the wavelets are diagonally entered in the model, with a 45° angle, so that the pulse orientation generates the most unfavorable load on the piles.

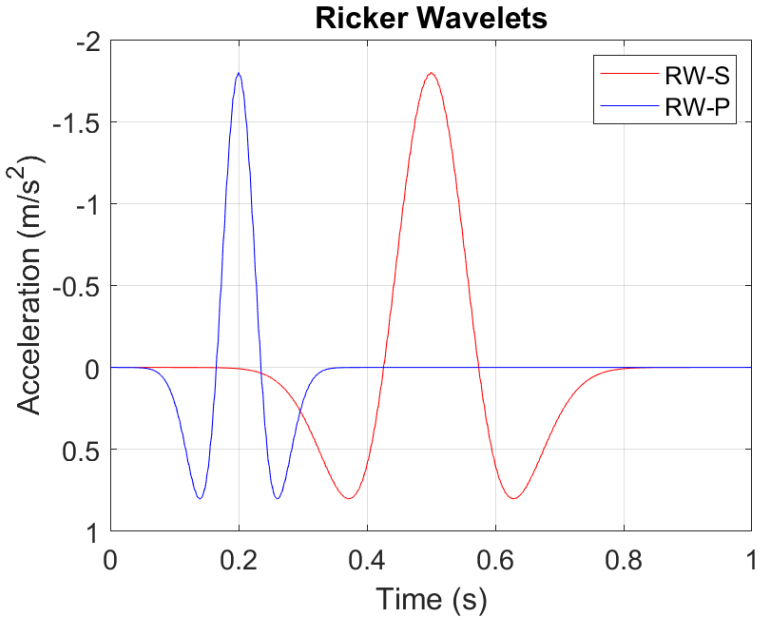

Figure 9 RW-S (red) and RW-P (blue) are used as input in configuration 1 of the model.

Table 10 Frequency and Duration of Ricker Wavelets.

Ricker Wavelet	Main Frequency (Hz)	Duration (s)	Amplitude (m/s2)
RW-S	3.04	0.5	1.52
RW-P	6.46	1.0	1.53

5.3.2 Seismic Input Description

To enhance the analysis of dynamic behavior, it was determined to include a scenario with seismic input. As mentioned before, the excavation fraction's (Model Configuration 1, Figure 7) inability to execute the input, it was opted to simulate a full excavation (Configuration 2, Figure 8). As the numerical model was developed to reproduce very stiff elastic conditions at its base (i.e. approximated bedrock), only strong motions recorded in rock stations are adequate.

On the other hand, the seismic event chosen is one previously used by Salas (2017), the Mw 8.8 earthquake that struck Maule, Chile in February 2010, recorded in rock station Rapel in two directions. The motions were scaled at the base of the model until achieving a value at the surface consistent with soil observations provided by the free-field soil record located in Santiago, where the soil exhibits almost the same geomechanical characteristics as the Santiago gravel previously described. The seismic input for North-South (N-S) and East-West (E-W) directions is depicted in Figure 10.

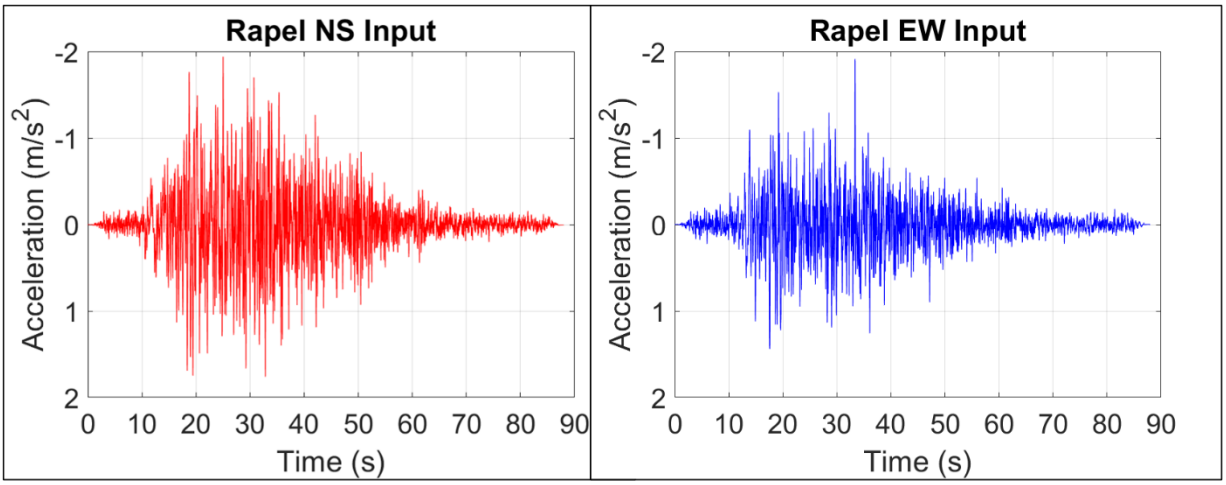

Figure 10 Ricker Pile wavelet (blue) and Ricker Soil wavelet (red) used as input in configuration 1 of the model.

6 Static Analysis Results

Because of the model symmetry shown in Figure 7, Groups 1 and 2 of piles share the same results hence, for an optimal presentation of results, only those of Group 1 are shown. The results of piles 1 and 2 are not shown to avoid inaccuracies in the result because of its boundary conditions (border piles).

6.1 Static Soil Pressure acting on Piles

An interface is used between the pile and the soil to extract the pressure acting on the piles through each construction stage.

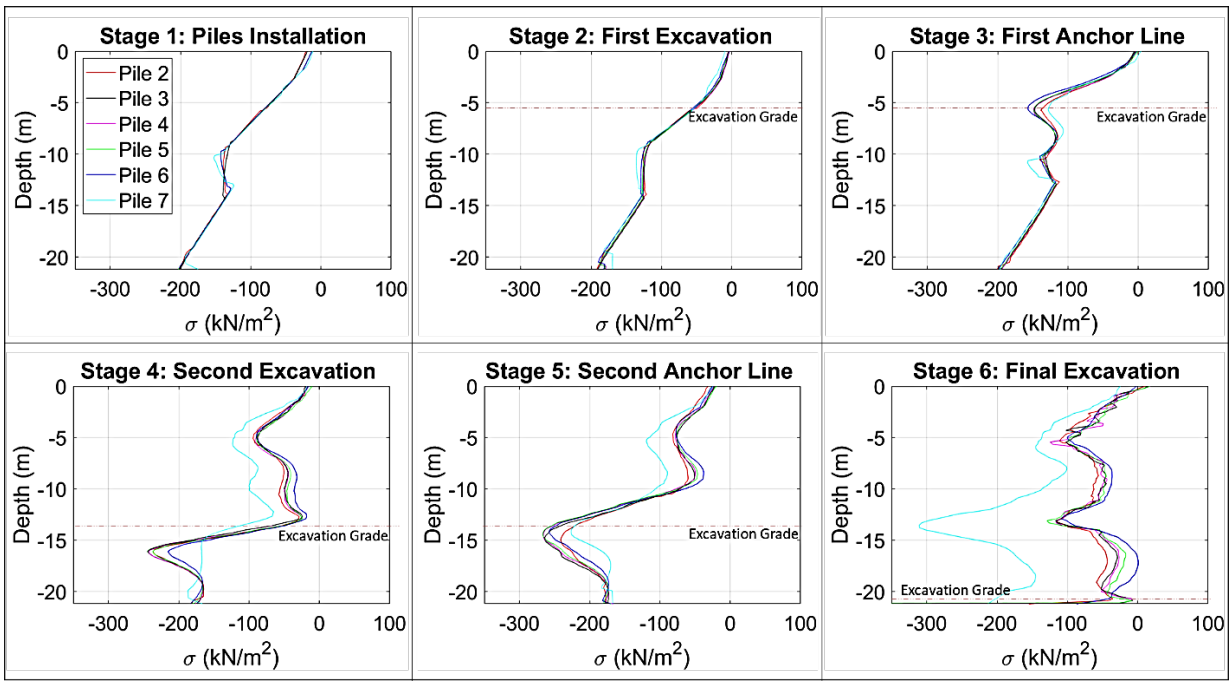

Figure 11 Static pressure acting on piles throughout the constructive stages.

From the FE model results Figure 11 shows the evolution of the lateral earth pressures applied on the point farthest from the excavation, induced by the sequential excavation. At an initial phase, the calculated lateral pressure is the same as the geostatic soil pressure for all the piles because a K0-based procedure was selected to initialize stresses in the FE model. Once the first anchor line is tensioned

(Stage 3), a stress concentration appears because of the local compressive stress produced by the tensioning process. At this point, the corner pile has a higher stress concentration compared to the other piles. The same effect is shown when the second anchor line is tensioned, increasing even more the difference between the corner pile and other piles. Moreover, it is observed that as the sequential excavation proceeds, the lateral earth pressure, except the zone near the anchors, tends to decrease for all the piles except for the corner pile, where the earth pressure reaches up to 3 times more compared to the rest of the piles. This phenomenon occurs due to the relaxation of stresses because of the lateral displacement of the piles and since the corner pile does not reach the same deformation levels as other piles.

6.2 Static Analysis of Displacement and Strain in Piles

The pile deformation throughout the construction phases is shown in Figure 12, it also presents the comparison between the in-situ inclinometer-measured deformation and the model deformation.

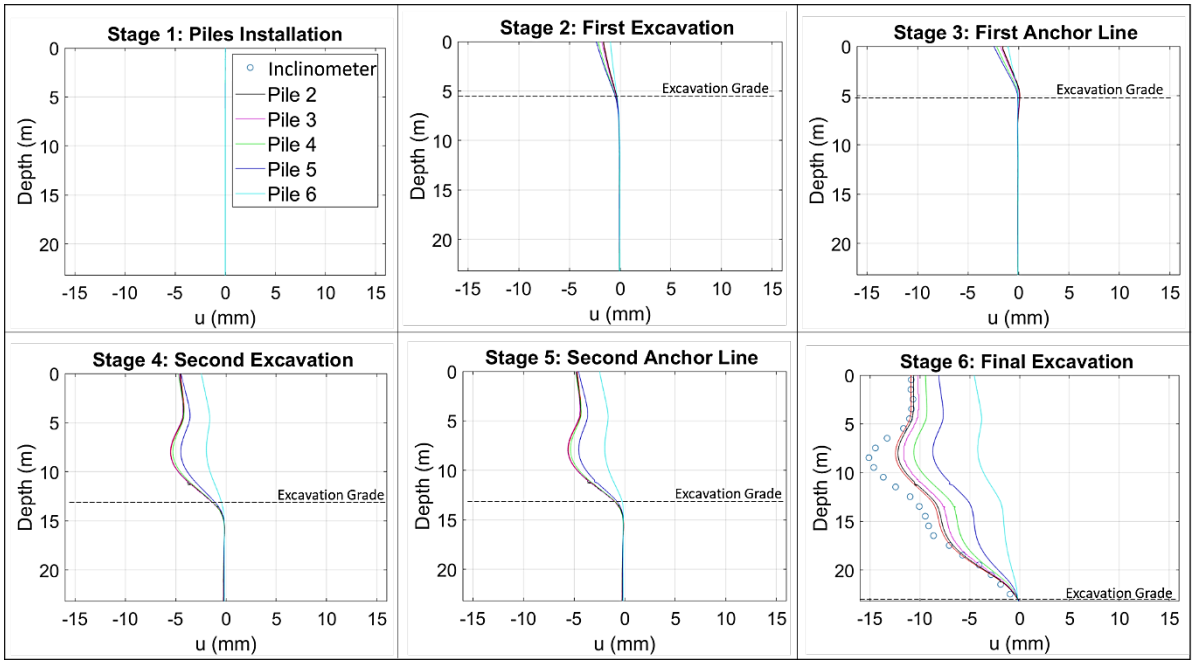

Figure 12 Piles deformation throughout the constructive stages.

At stage 2 and 3 show there's no significant effect of the corner pile on the other piles and consequently, there is no convergence in the results. Pile 7, in the excavation corner, deforms less than its neighbors since it is considerably constrained by the lateral soil. In these phases, the maximum superficial displacement reaches 2.36 mm and 2.44 mm for piles 5 and 6, respectively.

From Stage 4, the piles are less constrained by the soil, and the convergence begins to be noticed in the displacement of the piles located far from the corner pile. In this construction stage and in Stage 5 it can be noted that pile 6 is the only one influenced by the corner pile, while the other piles (2-5) show greater horizontal displacement. The maximum displacement for these stages is 4.50 mm and 4.67 mm, respectively. These values are found at a depth between the first and second anchor lines.

In stage 6, the corner pile effect influences up to pile 4, obtaining surface displacement in the range of 4.55 mm (in the corner) to 10.88 mm for piles 2 and 3. The maximum displacement is 12.43 mm at 8 m depth for piles 2 and 3.

The in-situ inclinometer measurement of a pile ubicated at sixteen spacings from the corner, assuming that, at that point, the corner effect is null. Comparing the in-situ measurement with the final phase displacements, it is shown that the first 6 m and last 5 m are almost identical to the in-situ measurement, while a maximum difference of about 18% is reached at 8.5 m depth. This variation in results may arise

due to several factors. Firstly, it could be attributed to the parameters employed for modeling Santiago gravel, which was originally calibrated for the 3D model developed by Salas (2017). It's important to note that Salas' model focused on a narrower section of the excavation, utilizing only two half piles. Secondly, the differences may also stem from the inability to fully replicate the anchor loads or from the inherent variability of the materials, which the model does not fully account for.

6.3 Bending Moment and Shear Forces on Piles.

The internal forces throughout all modeling phases for Group 1 piles are shown in Figure 13 and Figure 14.

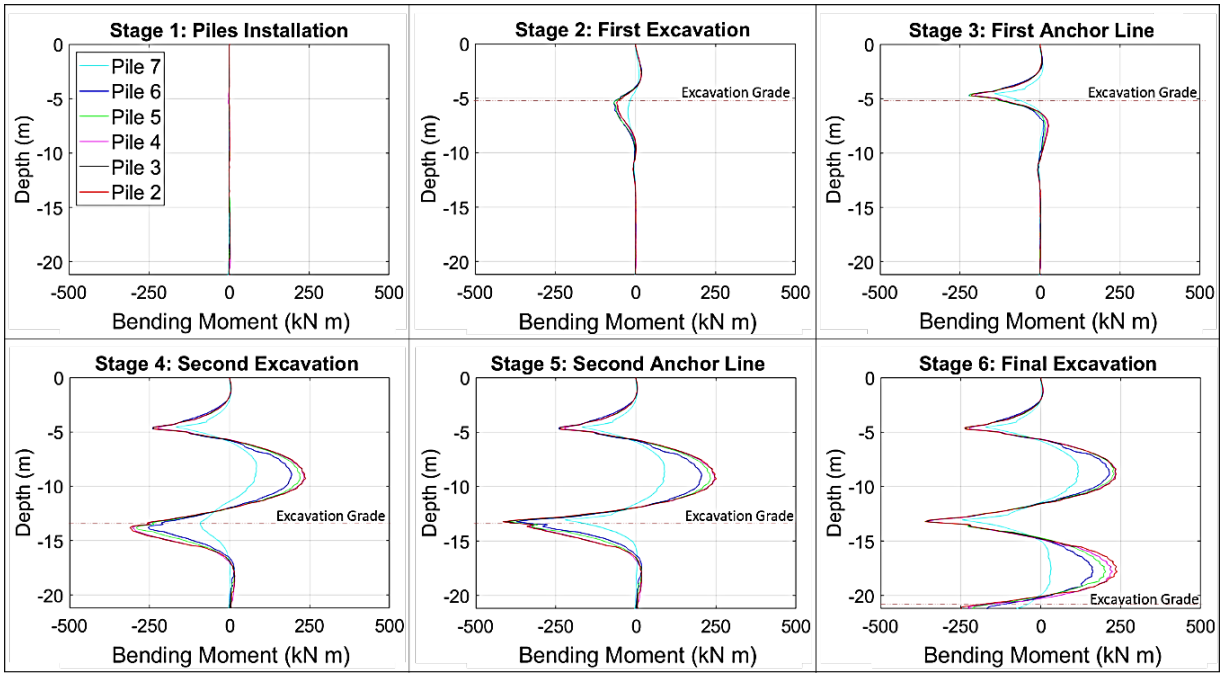

Figure 13 Piles bending moment throughout the constructive stages.

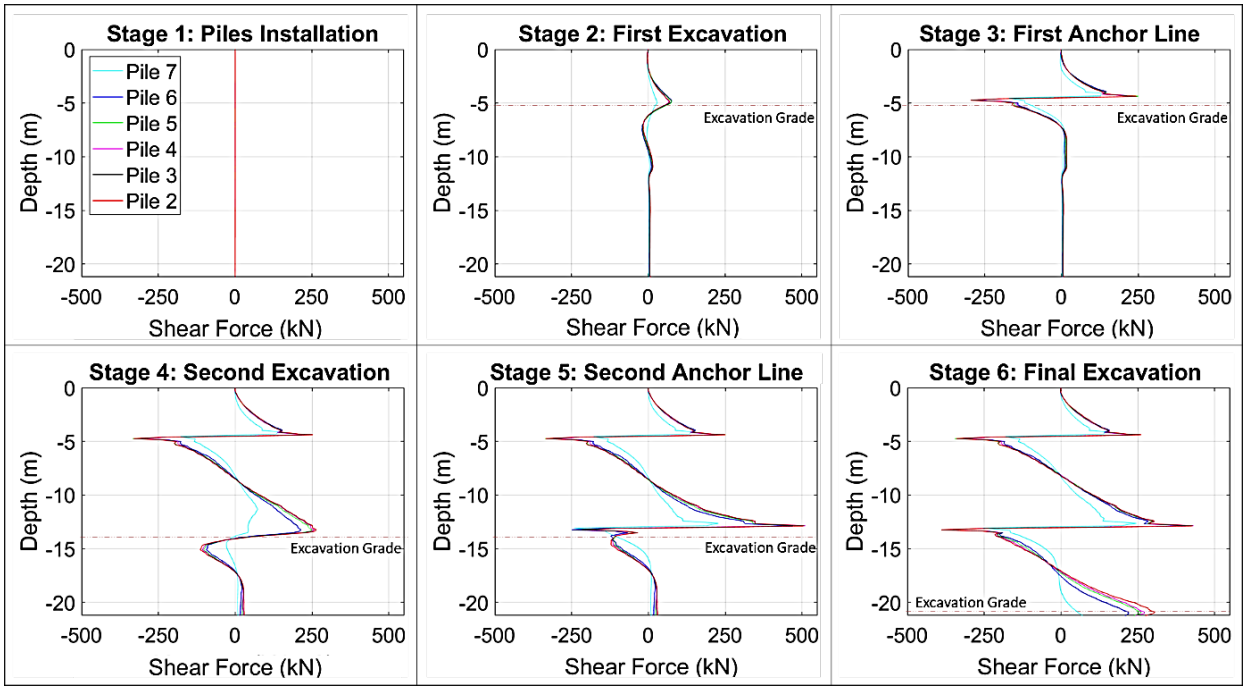

Figure 14 Piles shear force throughout the constructive stages.

The piles' bending moment and shear force through the stages of the excavation are displayed in Figure 13 and Figure 14. In the same way as for the displacement results, these graphics proved similar results for all the piles, except for the corner pile where, due to the restriction generated by the soil, the resulting bending moment and shear force are notably smaller. The maximum bending moment, located between the first and second anchor line on Stage 5 is about 251 kN*m for the converging piles (piles 2 and 3) while, for the corner pile, it is of 90 kN*m approximately.

On Stage 6, between the second anchor line and the final excavation, the maximum bending moment reaches 239 kN*m for the piles (piles 2 and 3) and 118 kN*m for the corner pile. Another point of interest is on Stage 5 for the piles (2 and 3) at the second anchor line depth where the bending moment a value of 362 kN*m is reached and, for the shear force, a value of 505 kN.

6.4 Pile Interaction Diagram

The interaction diagram (ID) shown in Figure 15 is generated using the usual reinforced concrete design criteria for the reference excavation pile with a longitudinal reinforcement of 14ϕ22 (14 steel bars with a diameter of 22 mm) and, the axial-moment from modeling stages as an envelope ID for each pile. Only the piles from Group 1 are presented in Figure 15 due to the model's symmetry.

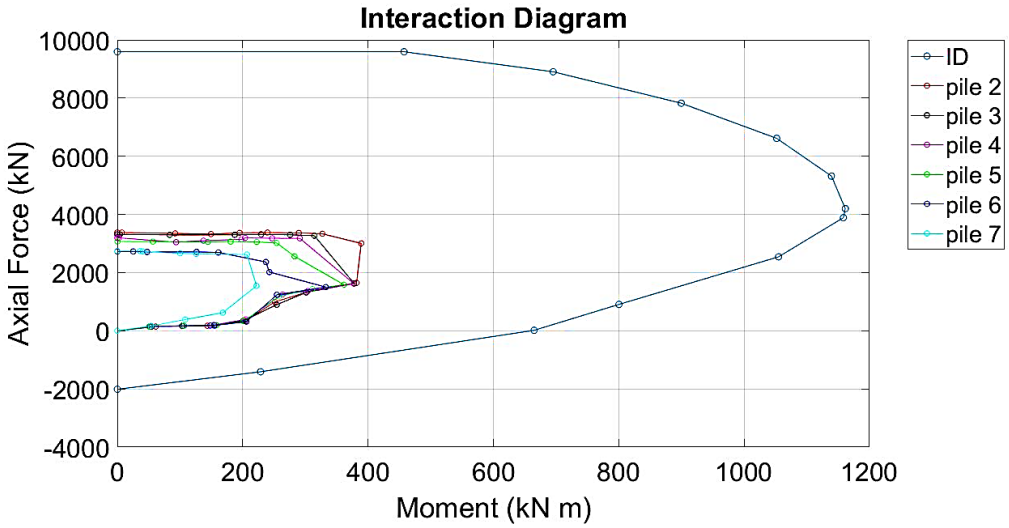

Figure 15 Piles Interaction Diagram.

As seen in Figure 15, the corner pile exhibits the lowest demand, with an increase in demand as the pile as the distance increases from the corner pile. However, it's important to note that the demand achieved is still far from the design failure limit.

6.5 Corner Pile

It is important to analyze the results of the corner pile since due to its greater deformation restriction, it does not deform as other piles in the excavation.

The corner pile develops less internal forces. Stage 6 develops a bending moment 50.6% lower than the value reached by the other piles, while the difference in shear force is about 39.7%. In this sense, as expected, the corner pile develops less deformation, reaching a maximum difference of 66.2% concerning the others, and therefore the soil around the pile is subjected to greater stress. Indeed, the soil pressures applied to the corner pile reach values of up to 329 kN/ m^2 at the second anchor line depth, in the last construction phase, being three times higher compared to other piles.

6.6 Comparison between Configuration 1 and 2 Static Analysis

When performing the static analysis of Configuration 2 across its construction stages and comparing it with the static analysis of Configuration 1, nearly identical results are obtained at all stages. Figure 16 and Figure 17 depict the comparison between the equivalent piles of both configurations (refer to Figure 7 and Figure 8 for equivalent piles) during the final excavation phase.

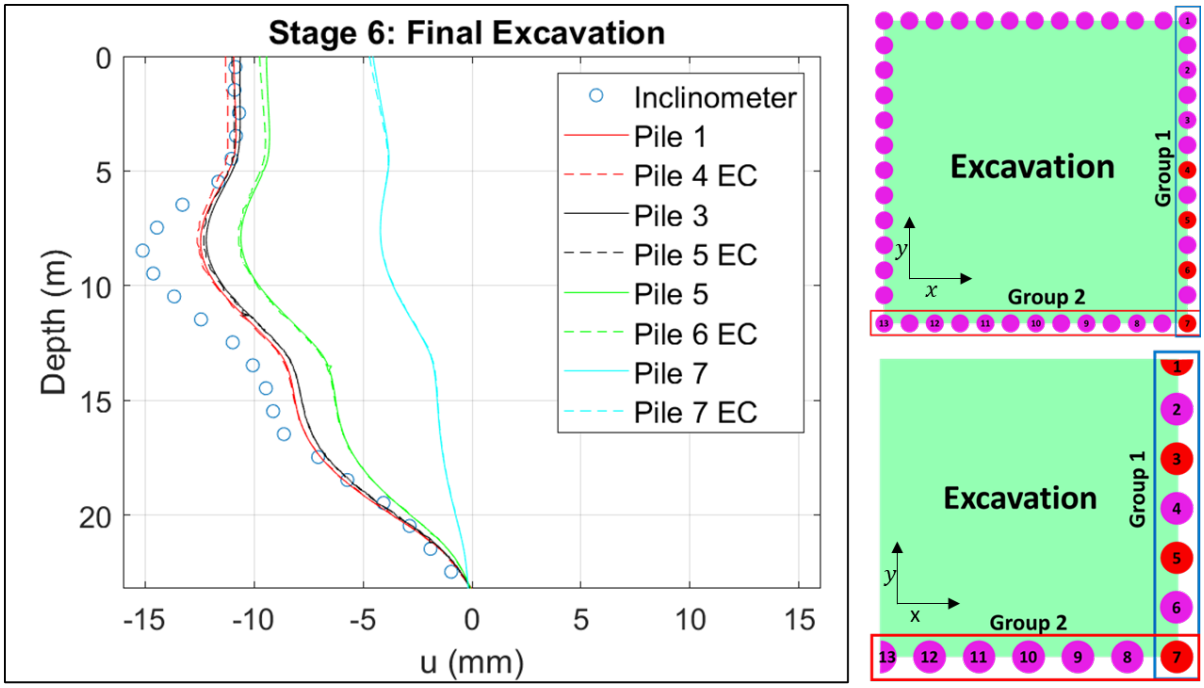

Figure 16 Piles displacement comparison between model configurations 1 and 2 at Stage 6 (EC=Equivalent Configuration).

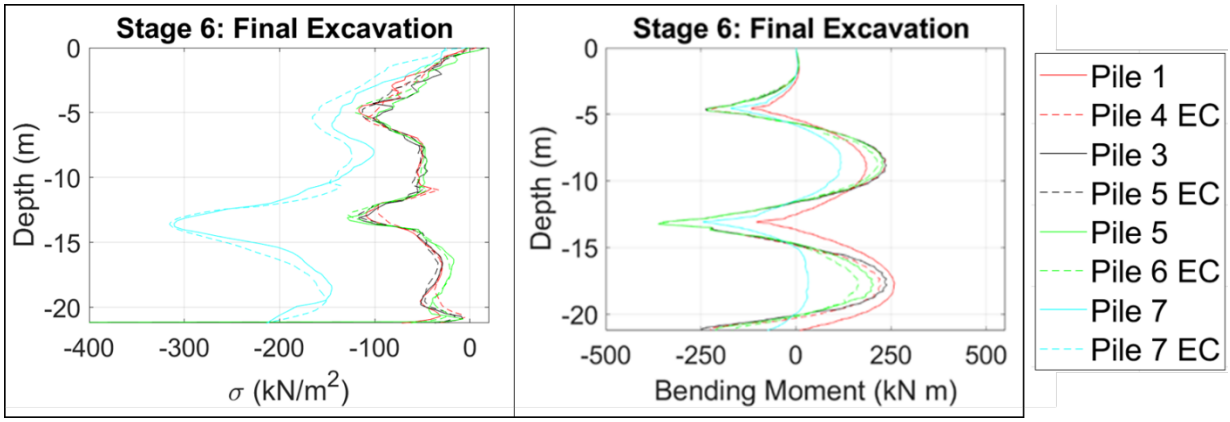

Figure 17 Pressure acting on piles and bending moment comparison between model configurations 1 and 2 at Stage 6.

These findings suggest that the dynamic response of the excavation fraction (Configuration 1) may be extrapolated to that of the complete excavation (Configuration 2), thereby enabling a comparison of responses to both Ricker inputs and the seismic input (Rapel 2D).

7 Dynamic Analysis Results

7.1 2D Ricker Wavelets Dynamic Response (Model Configuration 1)

The dynamic analysis involves running configuration model 1 under two scenarios using the Soil Ricker (RW-S) and Pile Ricker (RW-P) wavelets as described in 5.3.1. Despite the Ricker Pile and Ricker Soil lasting for 1 s and 0.5 s respectively, a computational run of 1.5 s divided into 30 phases of 0.05 s was considered for both.

Additionally, due to the symmetry of model 1, Groups 1 and 2 of piles (Figure 7) yield identical results in the static analysis. Consequently, only results from Group 1 are presented for clarity, except the border pile to mitigate boundary condition interference.

7.1.1 Free Field Response

In both cases, the response in the free field is measured approximately 20 m away from the corner of the excavation in the x-axis direction. Figure 18 displays the maximum displacement reached by the soil column throughout its depth and the corresponding time, for both cases.

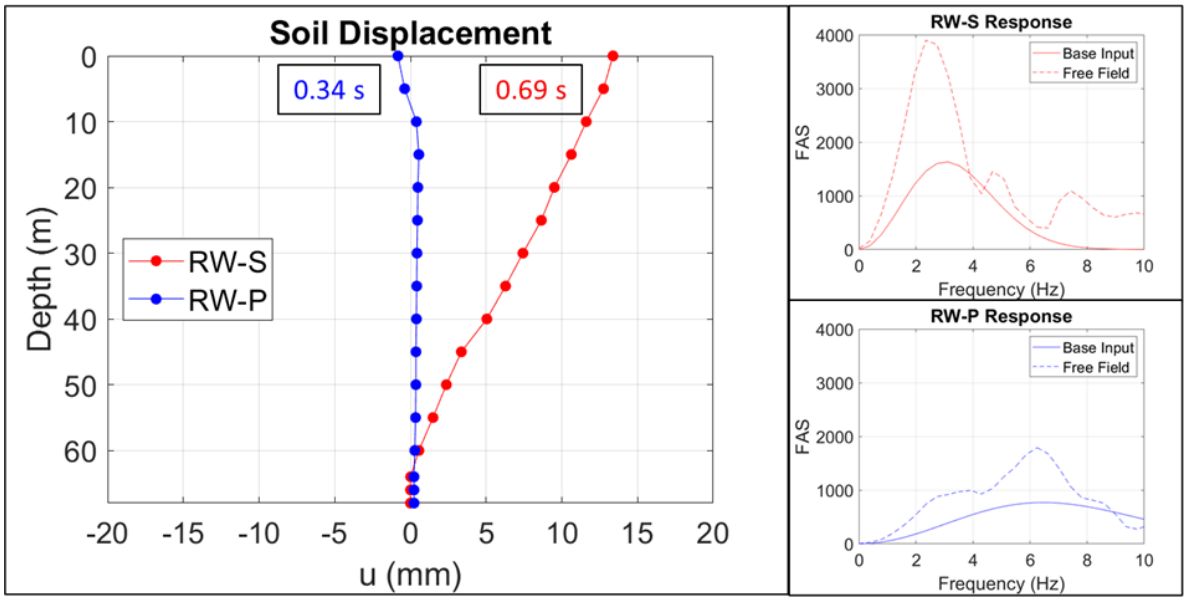

(a) (b)

Figure 18 Free field maximum displacement and FAS function for RW-P and RW-S input and free field response.

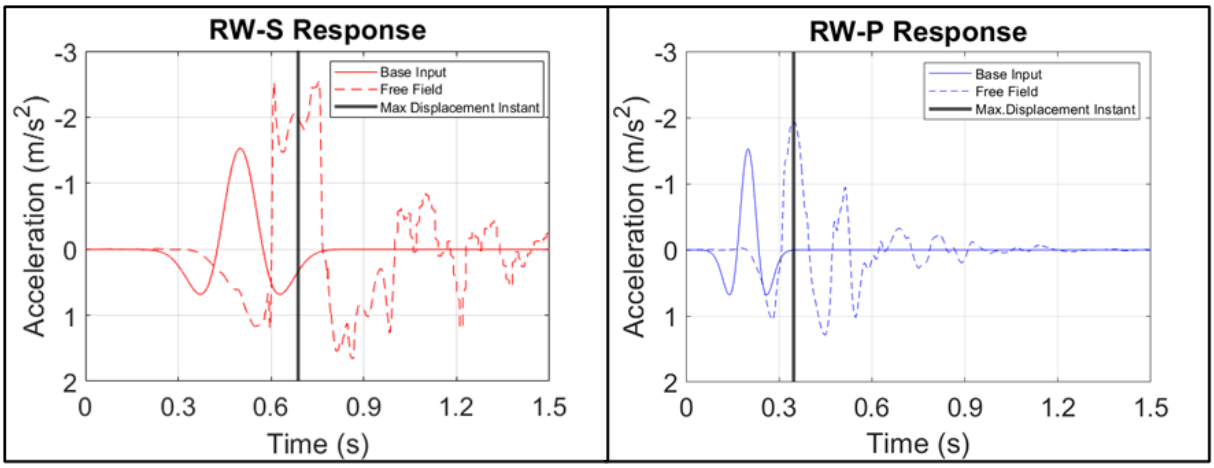

Figure 19 Free field response comparison between RW-S and RW-P scenarios and the maximum soil displacement instant.

It can be noted that the effect of the first synthetic wavelet (RW-S) on the soil column is greater than that caused by the second wavelet (RW-P). This observation aligns with expectations, as the input motion was tailored to the natural soil frequency to induce resonance and cause the most unfavorable scenario.

In the free-field response, Figure 19 (a) illustrates that the peak displacement occurs 0.35 s earlier for the RW-S than for the RW-P. This phenomenon may be attributed to the RW-S sharing its period with the natural period of the soil, facilitating faster transmission of motion.

It is noteworthy that while the RW-P free field response stabilizes at 1.5 s, the RW-S response continues to slightly oscillate. This is attributed to the model requiring additional runtime.

7.1.2 Maximum Pile Displacement Response

The pile displacement response achieved across the dynamic phases is presented in the following chapters for both Ricker wavelet cases. The two analyzed points of interest are the maximum and the residual response. The analyzed displacement only corresponds to the dynamic phases. For this stage, static displacements are considered zero.

The maximum pile displacement response achieved across the dynamic phases is presented in Figure 20 for both Ricker wavelet cases.

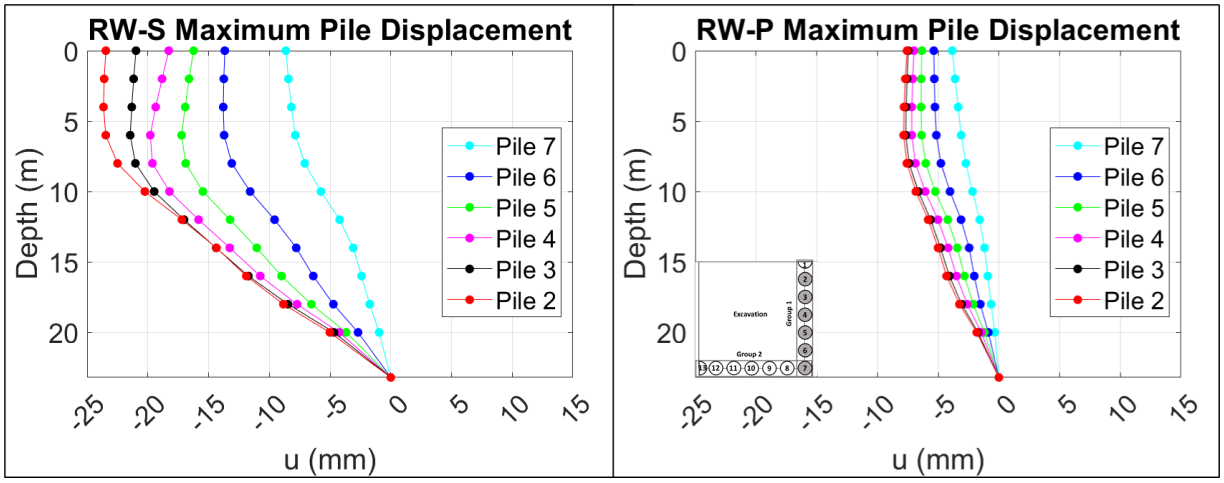

Figure 20 Maximum pile displacement for RW-S and RW-P occurred at 0.98 s and 0.58 s, respectively.

It is observed that the displacement induced by the RW-P signal, despite having the same frequency as the pile, is nearly three times smaller than that induced by the RW-S signal. In both cases, the maximum response occurs at the pile furthest from the corner (pile 2), at approximately 5.5 m depth, corresponding to the location of the first anchor line. Additionally, the corner pile (pile 7) experiences the greatest restriction relative to the other piles, as its corner position subjects it to constraints in both the x and y directions. The maximum displacement relative to the pile base is 23.65 mm for the RW-S case and 7.84 mm for the RW-P case. The larger displacement observed in the RW-S case is consistent with the fact that the wavelength of RW-S is 35.19 m, compared to 16.56 m for RW-P. Since the RW-S wavelength exceeds the excavation depth of 20.7 m, the system tends to move more akin to a 'rigid body,' which results in greater displacements.

In Figure 43 y Figure 44, presented in the appendix, a time-history graph for the pile heads in their unfavorable direction is shown.

7.1.3 Residual Pile Displacement Response

The residual displacement of the piles is presented in Figure 21 for both Ricker wave cases.

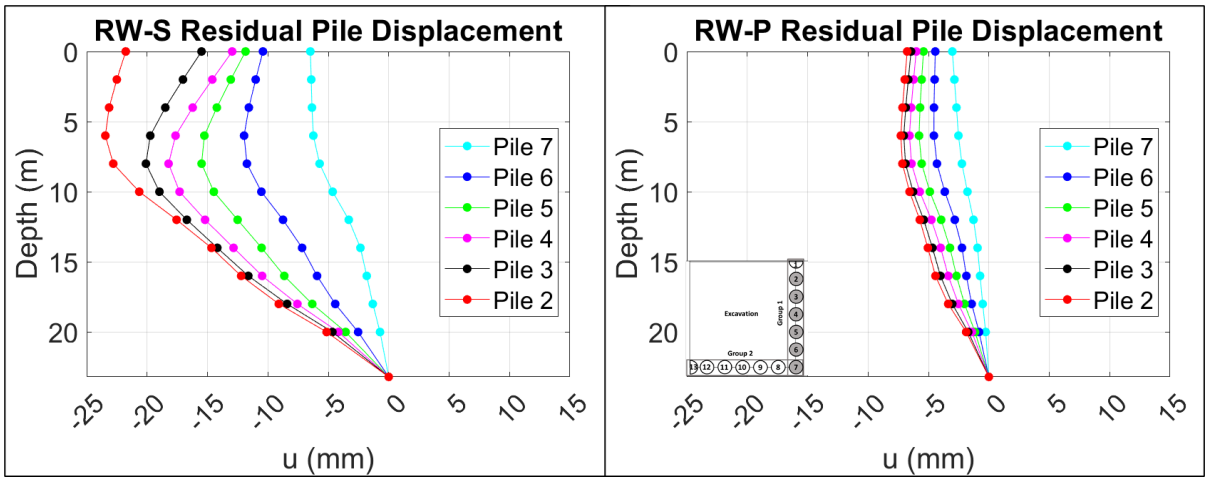

Figure 21 Residual pile displacement for RW-S and RW-P occurred at 1.50 s for both scenarios.

The presented figures indicate that the difference between the residual response of RW-S and RW-P differs by 0.5 mm and 0.8 mm, respectively, compared to their maximum response.

When comparing both free-field responses with those obtained in the piles, it is observed that the RW-S response reaches its residual displacement with an increase of 23.46 mm compared to its final static displacement for pile 2, while the RW-P response shows an increase of 7.29 mm. Furthermore, these displacement results are lower than the 40 mm post-seismic maximum displacement indicated by the NCh3206 standard for piles adjacent to streets, which is the case considered in the numerical model.

About the RW-S response, both the free-field response and residual displacement indicate that, at the end of the 1.5-second simulation, the piles were oscillating, and the displacement had not yet stabilized to its permanent state. Nonetheless, the free-field response demonstrates a tendency towards stabilization, suggesting that the residual displacement falls within a comparable range to that illustrated in Figure 21.

7.1.4 Dynamic Pressure on Piles

Unlike the pile displacements, both the soil pressure on the pile and internal forces were extracted for each dynamic phase; that is, for each 0.05 s interval, the internal force/pressure achieved at the end of each phase was obtained.

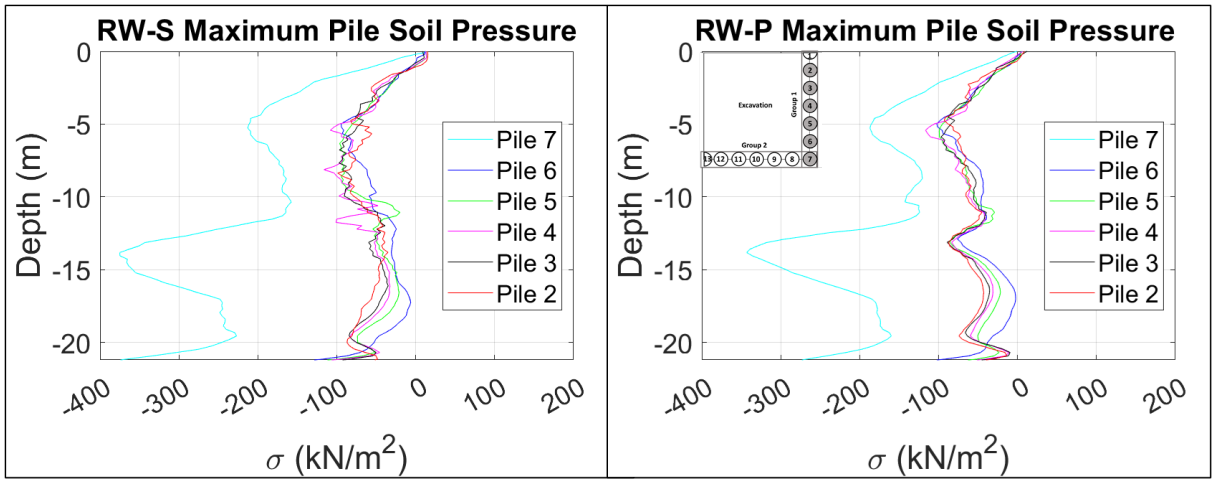

Figure 22 Maximum soil pressure on piles for RW-S and RW-P occurred at 0.85 s (phase N°17) and 0.50 s (phase N°10), respectively.

In both scenarios, the maximum pressure experienced by piles 2 to 6 exhibits minimal variation, while pile 7, positioned at the corner, demonstrates the highest soil pressure levels. Comparing the responses under both Ricker waves, the pressures exerted on piles 2-6 reach up to 110 kN/m^2. The notable distinction lies in the pressure applied to pile 7, where RW-S reaches up to 374 kN/m^2, while RW-P reaches 343 kN/m^2, at the same level at the depth of the second anchor line. Furthermore, in Figure 22, the greatest soil pressure difference between the corner pile (pile 7) and the others is recorded in the lower half, reaching up to 67 kN/m^2 for the RW-S case. These findings imply that soil pressure is predominantly concentrated on pile 7, both during static and dynamic phases, which is expected because this pile has greater restriction to deformation/and meets expectations since this stack's deformation is more restricted.

For further details, Figure 47 showing the dynamic pressures for Group 1 piles is presented in the Appendix.

7.1.5 Dynamic Bending Moment and Shear Forces on Piles

The maximum bending moment, i.e. where the absolute highest value is produced, reached during the dynamic phases, and its corresponding shear force, are depicted in Figure 23 and Figure 24 for RW-S and RW-P cases, respectively.

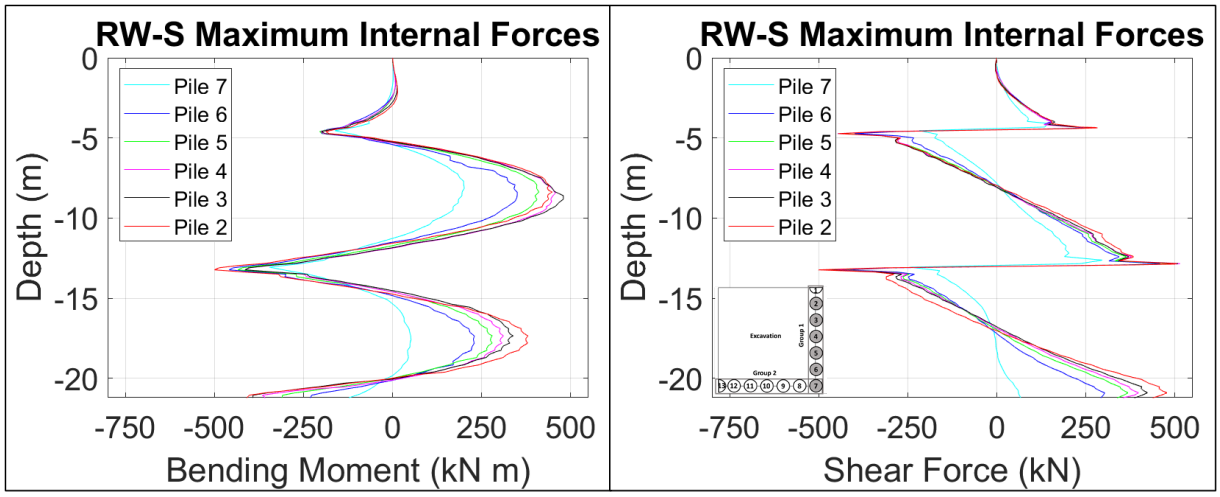

Figure 23 Maximum bending moment and corresponding shear forces for piles occurred at 1.5 s (phase N°30). RW-S scenario.

The RW-S results from Figure 23 indicate that at 1.5 seconds, the maximum bending moment is reached, which makes sense because, in the residual displacement (

), a visibly greater deflection is observed compared to the maximum displacement (Figure 20), consistent with the occurrence of the highest bending moment in this phase.

The maximum moment reached is 500 kNm at a depth of -13.5 m (second anchor line) for pile 2, and due to greater displacement restriction, the corner pile (pile 7) experiences the lowest maximum moment of 346 kNm. Compared to the static maximum bending moment, an increase of 38.12% is noted for pile 2.

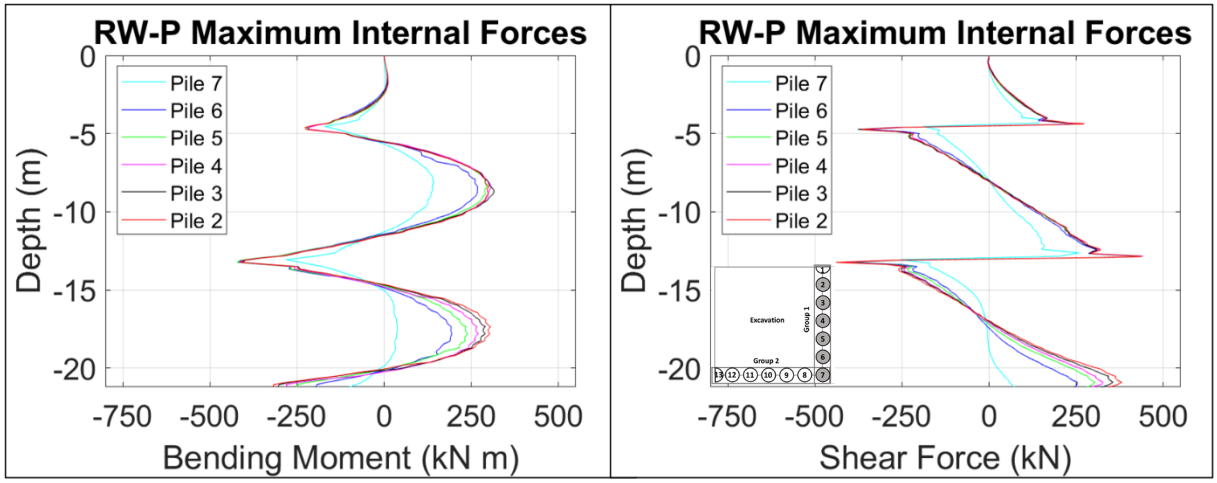

Figure 24 Maximum bending moment and corresponding shear forces for piles occurred at 0.6 s (phase N°12). RW-P scenario.

As expected, in Figure 24 it is observed, the maximum moment reached by RW-P is lower than that reached by RW-P, with a difference of 90 kNm. Similar to the RW-S results, the maximum moment reached is 410 kNm at a depth of 13.5 m (second anchor line) for pile 2. Due to greater displacement

restriction, the corner pile (pile 7) experiences the lowest maximum moment of 281 kNm. Although the seismic pressures induced are highest for pile 7, the increase in internal forces is minimal because its position at the corner allows for a redistribution of lateral earth pressure to adjacent piles and the lower deflection it experiences results in reduced internal forces. Compared to the static maximum bending moment, an increase of 13.26% is noted for pile 2.

7.2 Rapel 2D Dynamic Response (Model Configuration 2)

The dynamic analysis involves running model configuration 2 using Maule 2010, Chile seismic input recorded at Rapel station in the x-direction (NS) and the y-direction (EW), as described in section 3.3.2.

Soil pressure on the pile and internal force results were extracted for each dynamic phase. This means that for each 2.5-second interval, the internal force/pressure achieved at the end of each phase was obtained, indicating that smaller intervals may reveal greater maximum values.

It is important to note that due to the large number of piles modeled in this configuration, only 13 out of the 48 piles will be analyzed in this study. These 13 piles are located on the excavation half (see Figure 8) where the axis of seismic input symmetry lies and is separated into Group 1 (1-7) and Group 2 (7-13).

Group 1 comprises piles 1 to 7 and is predominantly affected by the Rapel NS input in the x-direction, whereas Group 2, consisting of piles 7 to 13, is primarily influenced by the Rapel EW input in the y-direction. For clarity, please refer to Figure 8 and Figure 16. Both maximum and residual displacement responses are examined. The analysis exclusively focuses on the dynamic phases, with static displacements considered zero at this stage.

7.2.1 Free Field Response

Same as in the Ricker Wavelet cases, the response in the free field is measured approximately 20 m away from the corner of the excavation, considering the resultant between the measured response in the x-direction and the y-direction. Figure 25 displays the maximum displacement reached by the soil column throughout its depth and the corresponding time, induced by Rapel NS and EW.

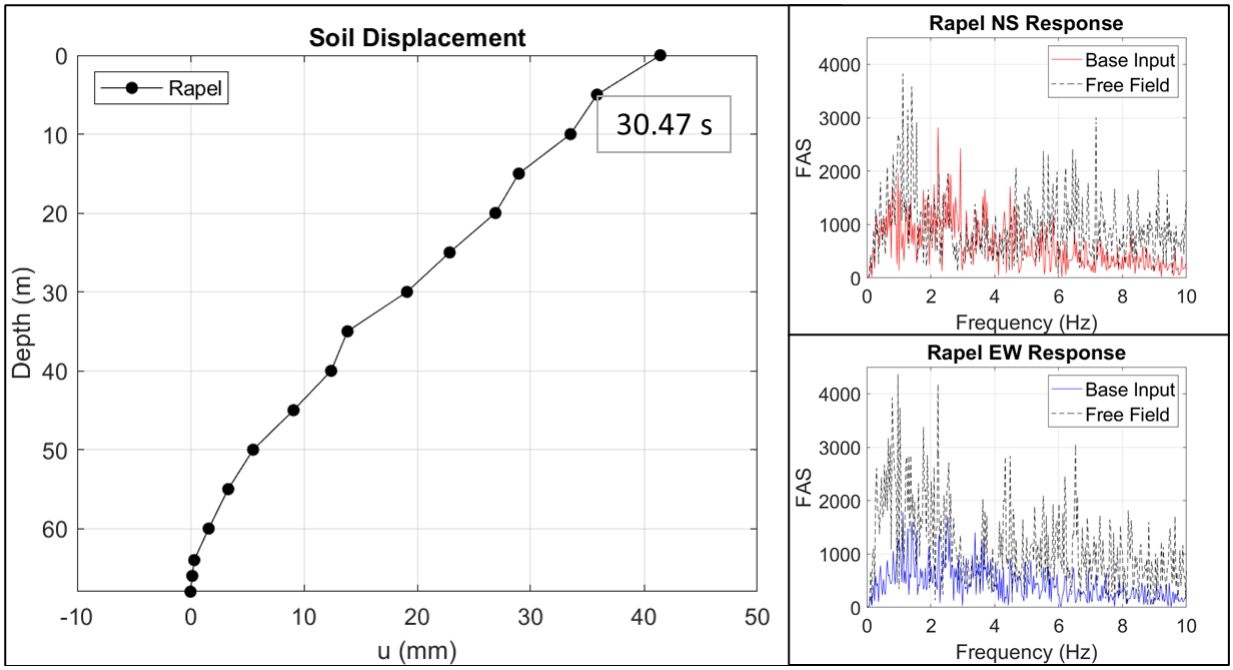

Figure 25 Free field maximum displacement and FAS function for Rapel NS and Rapel EW input and free field response.

The seismic impact on the soil column surpasses that induced by the RW-S (synthetic signal with identical frequency to that of the soil), reaching a displacement of up to 41.44 mm concerning the soil base. This displacement is approximately 8.8 times greater than that observed with the RW-S soil displacement.

In the free-field response, Figure 25 illustrates that although the Rapel NS waveform has a higher amplitude and the x-component (NS) is greater than the y-component (EW), the Fourier Amplitude Spectrum (FAS) function indicates that the Rapel EW component has a higher amplification than Rapel NS, but despite having a higher amplification, it does not compensate for the higher amplitude of NS.

Both the Rapel NS and EW responses probably continue to exhibit slight oscillations at the end of the simulation. This behavior could be attributed to the model requiring additional runtime, which was unfeasible due to the substantial computational demands of the model, even for the given seismic duration.

7.2.2 Maximum Pile Displacement Response

The response of pile displacements during the dynamic phases is detailed in the following sections for Group 1 and Group 2. Both maximum and residual displacement responses are analyzed, with emphasis on the dynamic phases, while static displacements are assumed to be zero at this stage. Figure 26 illustrates the maximum pile displacement response observed across the dynamic phases for both pile groups.

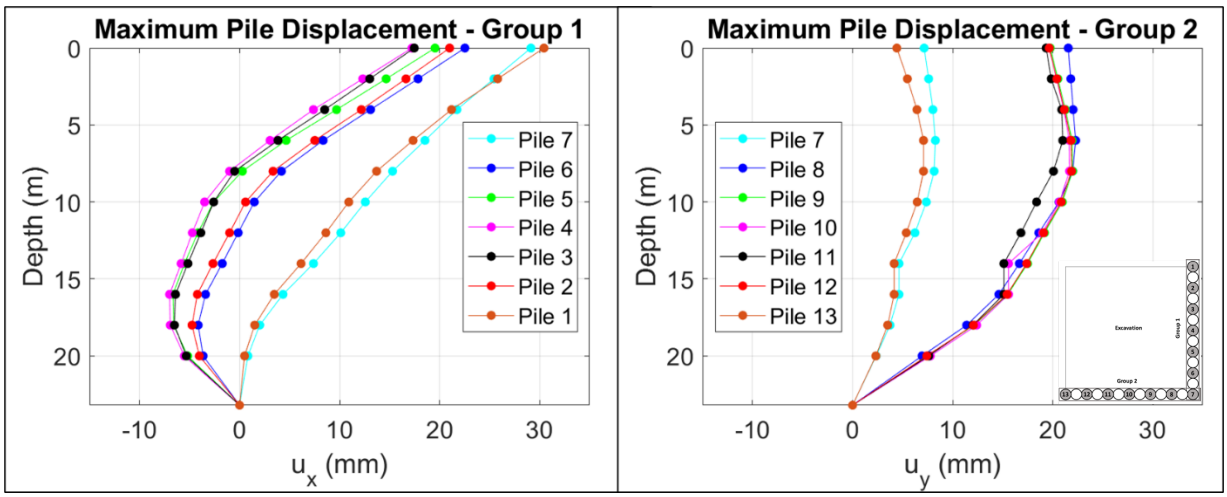

Figure 26 Maximum pile displacement for piles Group 1 and Group 2, occurred at 35.54 s and 34.58 s, respectively. Rapel earthquake input.

It is observed that both groups exhibit greater total displacements than in the Ricker waves cases, prompting a comparison and analysis of the maximum displacements between the base and head of the pile. Upon comparing these maximum displacements, it is noted that the piles reach up to 30.43 mm and 22.34 mm for Group 1 and Group 2, respectively. The higher displacement achieved by Group 1, mainly influenced by the Rapel NS input with the highest amplitude in both input and free-field response, is noteworthy. It is worth mentioning that the magnitude of the maximum displacement is similar to that obtained in the RW-S case, where it reaches 23.64 mm.

Group 1 shows its highest displacements at the heads of the corner piles (1 and 7), unlike the observations from the static analysis and the Ricker wavelet (RW) cases. Conversely, the other piles (2-6) exhibit maximum surface displacements ranging from 19.79 to 23.59 mm. It is noteworthy that the displacements tend to converge to a similar value as they move away from the corner piles, with nearly identical results observed for piles 3-5.

Meanwhile, Group 2 exhibits its greatest displacements for piles 8-12, reaching up to 22.34 mm near the depth of the first anchor line. On the other hand, corner piles 7 and 13 are mostly restricted in the y-direction, unlike corner piles 1 and 7 of Group 1 in the x-direction. This contributes to the aforementioned observations and reaffirms that the piles of Group 1 (in the x-direction, influenced by Rapel NS) represent the most unfavorable scenario. Additionally, it is observed that piles 8-12 do not display a converging displacement pattern as they move away from the corner, as they practically exhibit identical displacements among them.

In Figure 45 y Figure 46, presented in the appendix, a time-history graph for the pile heads in their unfavorable direction is shown.

7.2.3 Residual Pile Displacement Response

The residual pile displacement is presented in Figure 27 for both pile groups due to Rapel input in the x-direction (NS) and in the y-direction (EW).

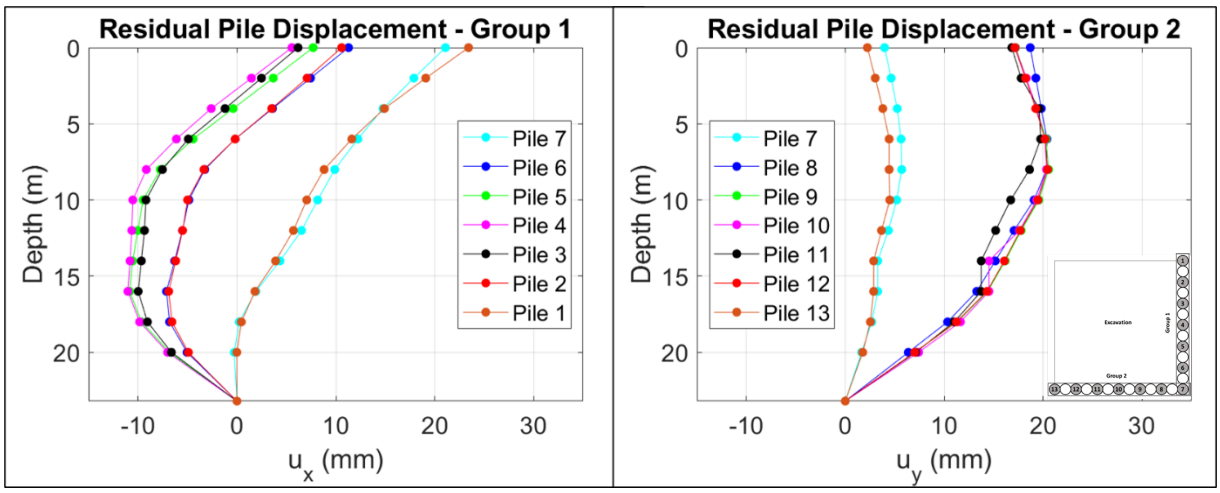

Figure 27 Residual pile displacement for piles Group 1 and Group 2, occurred at 87.96 s. Rapel scenario.

The presented figures indicate that the difference between the residual response of Group 1 and Group 2 differs by 7.03 mm and 1.97 mm, respectively, compared to their maximum response. Furthermore, these displacement results are lower than the 40 mm post-seismic maximum displacement indicated by the NCh3206 standard for piles adjacent to streets, which is the case considered in the numerical model.

Regarding the observed behavior, the trend observed in the maximum displacements is maintained. The residual displacements of Group 1 piles are located at the surface, with the highest displacement occurring at corner pile 1, and piles 2-6 showing some degree of convergence as they move away from the corner piles. Group 2 piles exhibit their greatest residual displacement at the depth of the first anchor line for piles 8-12, which practically display the same displacement. Meanwhile, corner piles 7 and 13 present the smallest displacements.

It is observed that corner piles 1 and 7 of Group 1 (in the x-direction) exhibit greater displacement than corner piles 7 and 13 of Group 2 (in the y-direction), thereby continuing the trend that the Rapel NS input in the x-direction, due to its higher amplitude, results in Group 1 being subjected to the most unfavorable conditions.

7.2.4 Dynamic Pressure on Piles

Unlike the pile displacements, both the soil pressure on the piles and internal forces were extracted for each dynamic phase.

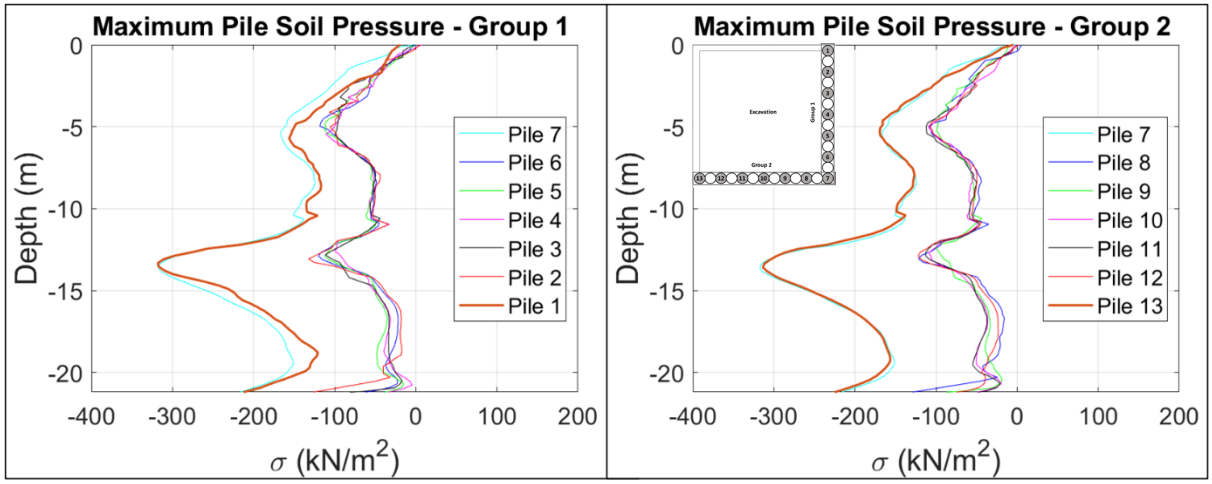

Figure 28 Maximum soil pressure on piles for Group 1 and Group 2 occurred at 7.5 s (phase N°3). Rapel scenario.

For both scenarios, the corner piles (1, 7, and 13) exhibit the highest soil pressures, with Group 1 recording 362.19 kN/m^2 and Group 2 showing 338.46 kN/m^2, while the remaining piles range from 107.55 to 138.90 kN/m^2. These maximum pressures occur at the depth of the second anchor line.

It is noted that these maximum pressures are almost attained under static conditions, corresponding to the initial seconds of the Rapel earthquake. Throughout the subsequent dynamic phases, slight variations in soil pressures are observed, particularly in the corner piles, but they do not surpass the final static pressure. This observation complements the displacement data, indicating a greater displacement capacity across all piles.

Unlike what was observed in the Ricker wavelet cases, in these results, the dynamic soil pressure is not concentrated solely on the corner piles. This may be due to the higher displacements reached and also possibly because the model represents a complete excavation, leading to redistribution across all four corner piles in the model.

For further details, Figure 48 showing the dynamic pressures for Group 1 piles is presented in the Appendix.

7.2.5 Dynamic Bending Moment and Shear Forces on Piles

The maximum bending moment reached during the dynamic phases, and its corresponding shear force, are depicted in Figure 29 and Figure 30 for piles Group 1 and Group 2, respectively.

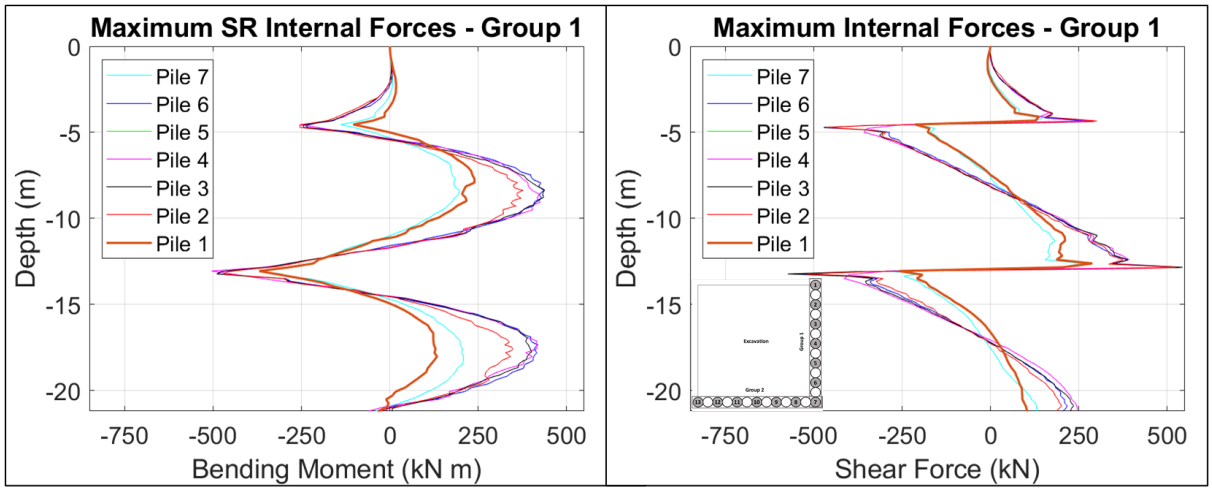

Figure 29 Maximum bending moment and corresponding shear forces for Group 1 piles occurred at 65 s (phase N°26). Rapel scenario.

The Group 1 results from Figure 29 indicate that at 65 seconds, the maximum bending moment of 504.34kNm is reached at the second anchor line depth for pile 4, and due to greater displacement restriction, the corner pile 7 experiences the lowest maximum moment of 359.01 kNm. Compared to the static maximum bending moment, an increase of 38.12% is noted for pile 4.

It is noted that slightly higher internal forces are reached compared to those obtained in the RW-S case, which aligns with the observations made in the displacements as well.

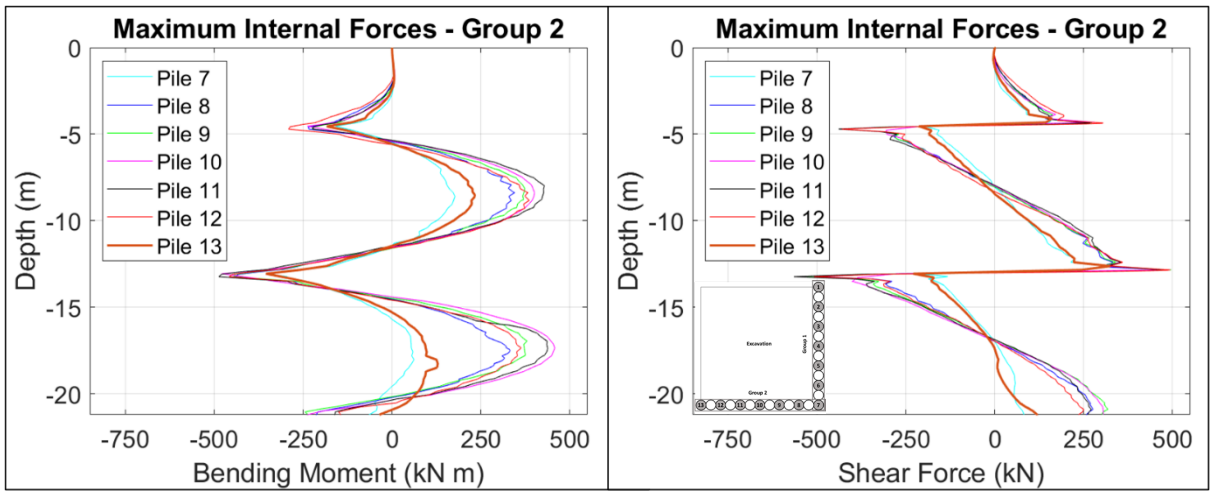

Figure 30 Maximum bending moment and corresponding shear forces for Group 2 piles occurred at 65 s (phase N°26). Rapel scenario.

The Group 1 results from Figure 30 indicate that at 65 seconds, the maximum bending moment of 487.28 kNm is reached at the second anchor line depth for pile 11, and due to greater displacement restriction, the corner pile 7 and 13 experience the lowest maximum moment of 337.01 kNm. Compared to the static maximum bending moment, an increase of 34.60% is noted for pile 11.

As expected, the maximum moment reached by Group 2 is lower than that reached by Group 1 and RW-S results, with a difference in the range of 12.58-17.06 kNm.

7.3 Comparison with NCh Design

The induced dynamic envelope soil pressures and the dynamic envelope internal forces are compared with those obtained through the Mononobe-Okabe (MO) calculation and the Chilean standard NCh433 Of. 2009 for the piles that exhibit the most unfavorable scenario. This comparison is conducted for the RW-S and Rapel scenarios due to their higher results in dynamic analysis.

7.3.1 Dynamic-induced Lateral Soil Pressure on Piles

An envelope of dynamic-induced soil pressure values was generated from the profiles of the dynamic phases for each motion in Figure 31. These results are compared against the seismic-induced pressure applicable to permanently laterally restrained basement walls calculated according to the Chilean standard NCh433 Of. 2009, as well as against the Mononobe-Okabe's (M-O) earthquake-induced thrust theory, considering the recommendations of Seed & Whitman (1970) and using kh=0.12, 0.15 and 0.18, and kv=0.0. The range of the seismic coefficient used was chosen to include the coefficients obtained by Salas (2017), which are between 0.15 and 0.17.

These induced soil pressure values are compared for pile 1 in the case of RW-S and pile 7 in the case of Rapel.

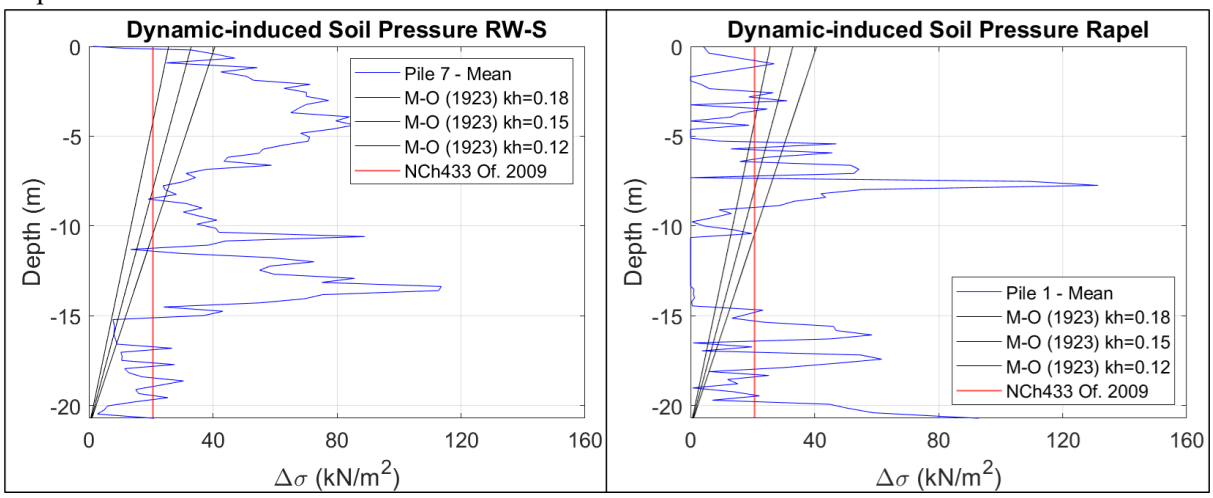

Figure 31 Envelope Dynamic-induced soil pressure, comparison between the reference code, means values calculated for each motion, and M-O theory for RW-S and Rapel.

In the RW-S scenario, the induced dynamic soil pressure exhibits 81.81% more than those calculated with the standard and 89.26% more than those calculated with M-O in the between-anchor lines zone, the mid-section. In the rest of the pile, the envelope of dynamic-induced soil pressure values is lower than those obtained using the standard and MO.

The induced dynamic thrust due to the seismic input of Rapel generally results in lower magnitudes compared to RW-S, except at one point. In the mid-section, between anchors, there is no induced soil pressure, while in the upper zone, it exceeds the value calculated with the standard and is mostly lower than the calculated with MO. In the lower part, it surpasses the standard by up to 66.12% and MO by up to 89.67%.

Although both scenarios yielded similar displacement values, it is observed that the load induced by Rapel presents generally lower induced dynamic soil pressure in the analyzed corner piles. This can be explained by the observation that in the dynamic phases, in the RW-S scenario, the maximum soil pressure is concentrated on the corner pile (pile 7, see Figure 22) due to movement restriction, while in the Rapel scenario, the corner piles (piles 1, 7, and 13, see Figure 28) undergo greater displacement, resulting in lower-magnitude dynamic soil pressure.

7.3.2 Dynamic-induced Internal Forces in Piles

The envelope of dynamic internal forces is compared with those obtained through the Mononobe-Okabe (MO) calculation, with kh=0.15, and the Chilean standard NCh433 Of. 2009 for the piles exhibiting the most unfavorable scenario (Pile 2 and Pile 4). These forces for MO and NCh433 were obtained through the limit equilibrium method calculated by Salas (2017). This comparison is conducted for the RW-S and Rapel scenarios due to their higher dynamic analysis results.

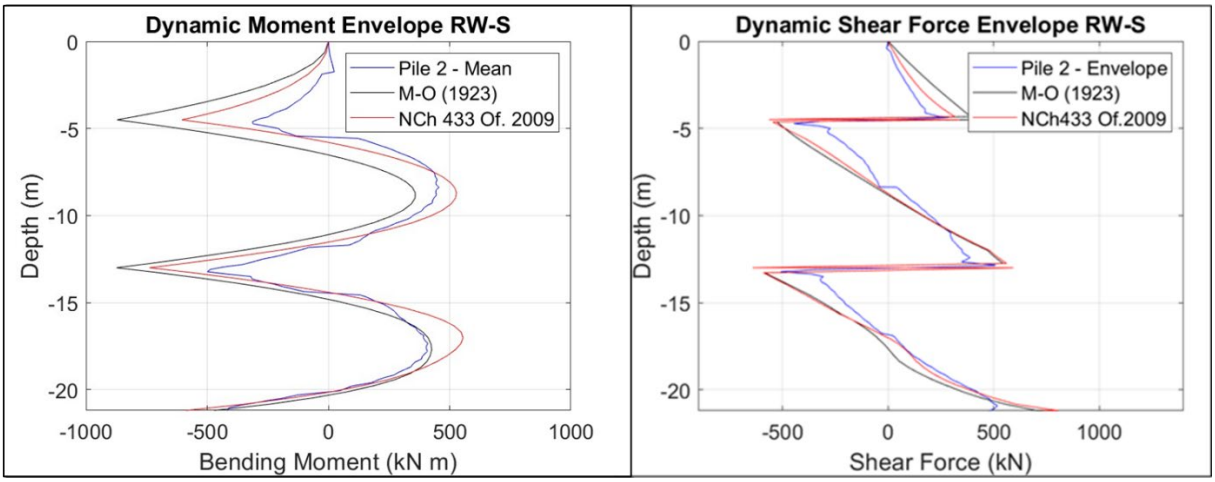

Figure 32 Bending moment and shear force comparison between dynamic envelope response and the results obtained after applying the reference code and the M-O surcharge load for the RW-S scenario.

Figure 32 shows that using MO yields higher negative bending moments, while the Chilean standard presents higher positive bending moment values. The dynamic envelope for the pile with the highest internal forces in the RW-S case exhibits a bending moment throughout its depth that is lower than MO by up to 64.14% and lower than the standard by up to 48.37% at a depth of 4.5 m depth (first anchor line).

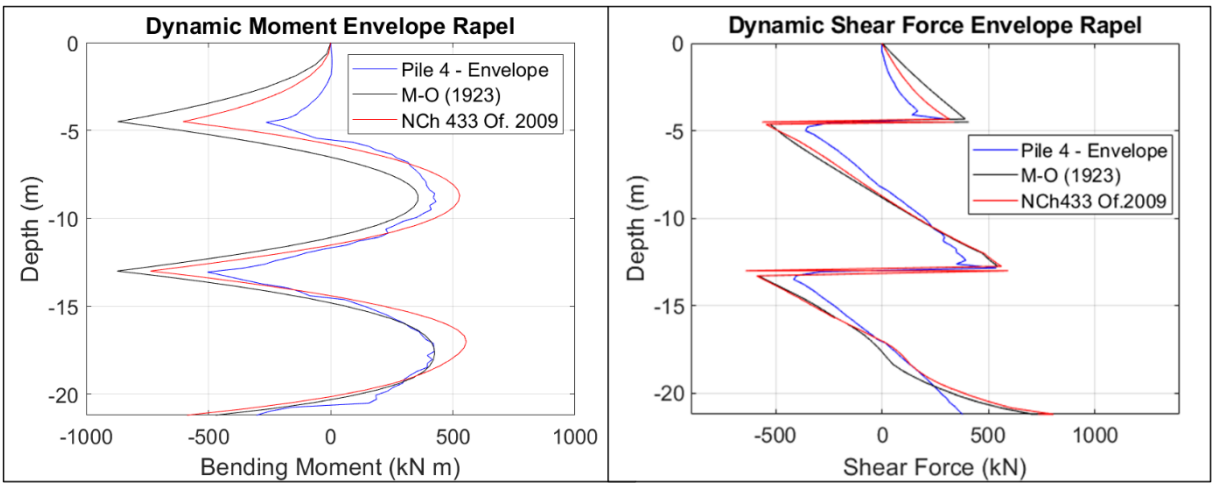

Figure 33 Bending moment and shear force comparison between dynamic envelope response and the results obtained after applying the reference code and the M-O surcharge load for the Rapel scenario.

Similarly to the RW-S case, in Figure 32, it is observed that the dynamic bending moment envelope obtained is lower than the standard and MO, by up to 69.76% and 53.39%, respectively, at a depth of 4.5 m depth. Consequently, it is noted that the dynamic internal forces calculated from MO and the standard achieve results that, at least in the analyzed models, contain the developed dynamic envelope.

8 Conclusions

In conclusion, the findings of this study provide valuable insights into the static and dynamic behavior to which the piles of a shoring system are subjected.

From the static analysis of both configurations, it is concluded that as the piles move away from the corner pile, they tend to have similar displacement, internal forces, and thrust. Meanwhile, the corner pile, due to its greater movement restriction, has the lowest displacement and therefore lower internal forces than the other piles, up to 66.37% lower, and experiences a higher soil thrust demand on it, up to 63.83% higher at the bottom of the pile.

Regarding the dynamic analysis conducted in the RW-S and RW-P cases, it is observed that despite using a Ricker wavelet with a main soil frequency and another according to the pile, the Ricker wavelet with the same frequency as the soil (RW-S) generated greater displacements, soil pressure, and internal forces. Therefore, it can be concluded, For this model, the soil frequency induces the most unfavorable scenario compared to the pile frequency. This is because when a system vibrates at or near its natural frequency, resonance effects occur, leading to amplified responses. In this case, the soil, which constitutes a larger portion of the system, plays a dominant role. As the frequency of the external excitation approaches the soil's natural frequency, the system experiences larger deformations and internal forces. In the RW-S scenario, the corner pile developed the greatest soil pressure, exceeding the others by up to 85.50%, i.e., the soil pressure is concentrated on this pile during the dynamic phase.

In the case of Rapel, although significantly higher results were expected compared to the RW-S scenario, both the generated internal forces and the maximum and residual displacements were similar in magnitude. Unlike what was observed in the RW-S and RW-P cases, Rapel does not exhibit dynamic soil pressure concentrated on the corner piles. Moreover, the maximum dynamic soil pressure is presented in the initial phases, practically corresponding to the static soil pressure. As for the values of maximum displacements and internal forces attained, they can be up to 22.31% higher than the displacements achieved by RW-S at the soil surface, and the forces can be up to 17.23% greater between the second anchor line and the excavation grade.

In the case of Rapel, although significantly higher results were expected compared to the RW-S scenario, both the generated internal forces and the maximum and residual displacements were similar in magnitude. Unlike what was observed in the RW-S and RW-P cases, Rapel exhibits lower dynamic soil pressure values, so although dynamic soil pressure is concentrated on the corner piles, it is lower than that observed in RW-S. Moreover, the maximum dynamic soil pressure is presented in the initial phases, practically corresponding to the static soil pressure. As for the values of maximum displacements and internal forces attained, they can be up to 22.31% higher than the displacements achieved by RW-S at the soil surface, and the forces can be up to 17.23% greater between the second anchor line and the excavation grade.

In this case study, the dynamically induced soil pressure from the RW-S and Rapel scenarios, particularly in the x-direction (NS), exceeded the dynamic soil pressure component calculated using MO and the NCh433 Of. 2009 standard in certain zones. The upper zone (0-5 m depth) and the area between anchor lines (5-13.5 m depth) exhibit the highest dynamically induced soil pressure of up to 113.64 kN/m^2 and 85.66 kN/ m^2 for RW-S, while Rapel shows its greatest soil pressure in the region between anchor lines (5-13.5 m depth) of up to 131.41 kN/ m^2 and the lower part of the pile (13.5-20.7 m depth) of up to 61.64 kN/ m^2.

The envelopes of the bending moment present lower values, both in the RW-S and Rapel scenarios, compared to the standard and MO, by up to 64.31% and 69.76% for each case at a depth of 4.5 m, (first anchor line). Consequently, it is noted that the dynamic internal forces calculated from MO and the standard achieve results that, at least in the analyzed models, encompass the developed dynamic envelope. However, it should be highlighted that both the Mononobe-Okabe (MO) method and the standard NCh433 have limitations in their applicability. While they provide a conservative approximation for induced dynamic forces, the dynamic thrust in NCh433 is intended for underground walls, and the MO method assumes a simple distribution of lateral pressures. Neither approach fully

captures the complexity of structures with anchorage systems. Therefore, further verification is required to determine if these methods apply accurately to other cases, particularly when dealing with deep excavations with anchors, where more complex interactions may occur.

Furthermore, the results indicate that this modeled excavation allows for lower pile displacements than those contemplated in the standard, resulting in a higher soil pressure load exceeding by up to 84.27% the value obtained from it at a depth of -7.7 m.

9 Recommendations

The study conducted by Salas (2017) replicates the discontinuous anchored pile support system behavior in a pseudo-3D model by calibrating parameters for Santiago's gravel using the HS Small Strains constitutive model, and by modeling anchoring stress equivalent to that employed in the actual excavation, of the current research did not achieve a satisfactory characterization of anchor behavior, despite employing the same parameters for modeling Santiago's gravel. Therefore, a more in-depth analysis may be necessary to elucidate the cause of this discrepancy, or parameter recalibration may yield more accurate results in replicating anchor behavior in a complete 3D model.

Another aspect that could enhance this study is conducting a sensitivity analysis, although this may significantly extend the computer runtime. The sensitivity analysis could assess various static characteristics of the corner pile, such as pile size and excavation depth, as well as the impact on other piles due to different anchoring tensions. Additionally, running models with more seismic signals could reveal patterns in the dynamic behavior and allow the development of equations to provide numerical approximations that could be applied to real cases.

It is advisable to conduct further analyses evaluating the geometry of a real excavation, as the cube shape may have generated strains in the corners that would not occur in a different excavation area.

Lastly, ideally, these structures should be instrumented to measure their dynamic behavior accurately to validate a numerical model reliably.

10 References

ARAVENA. (2020). ANÁLISIS DEL COMPORTAMIENTO SÍSMICO DE ENTIBACIONES EN SUELOS FINOS DEL SECTOR ORIENTE DE SANTIAGO.

BENZ, T. (2007). SMALL-STRAIN STIFFNESS OF SOILS AND ITS NUMERICAL CONSEQUENCES. IN UNIVERSITY OF STUTTGART.

BOLDRINI, S., & LÓPEZ, F. (2014). DISEÑO E INSTRUMENTACIÓN EN ENTIBACIÓN MEDIANTE PILOTES ANCLADOS EN LA GRAVA DE SANTIAGO.

BUSTAMANTE. (1986). A METHOD FOR CALCULATING ANCHORS AND INJECTED MIRCROPILES. BULLETIN OF THE SEMSC, A METHOD FOR CALCULATING ANCHORS AND INJECTED MIRCROPILES., 81–82.

CHEN, C. Y., & MARTIN, G. R. (2002). SOIL - STRUCTURE INTERACTION FOR LANDSLIDE STABILIZING PILES. COMPUTERS AND GEOTECHNICS, 29(5), 363–386.

EAB. (2008). RECOMMENDATIONS ON EXCAVATIONS. (P. DEUTSCHE GESELLSCHAFT FÜR GEOTECHNICK E.V., 2ND ED).

HARROP-WILLIAMS. (1989). ARCH IN SOIL ARCHING. JOURNAL OF GEOTECHNICAL ENGINEERING, 115(3), 415–419.

KHATAMI, H., DENG, A., & JAKSA, M. (2019). AN EXPERIMENTAL STUDY OF THE ACTIVE ARCHING EFFECT IN SOIL USING THE DIGITAL IMAGE CORRELATION TECHNIQUE. COMPUTERS AND GEOTECHNICS, 108(JANUARY), 183–196. HTTPS://DOI.ORG/10.1016/J.COMPGEO.2018.12.023

KORT, I., MUSANTE, H., & FAHRENKROG, C. (1979). IN-SITU MECHANICAL PROPERTIES MEASUREMENTS OF GRAVELLY SOIL USED IN AN INTERACTION AND FOUNDATION MODEL FOR THE SANTIAGO METRO. 6TH PANAMERICAN CONFERENCE ON SOIL MECHANICS AND FOUNDATION ENGINEERING, 217–224.

LÓPEZ, S., & SANHUEZA, C. (2019). ANÁLISIS DE LA DISTRIBUCIÓN DE EMPUJES DE SUELOS SOBRE ESTRUCTURAS DE CONTENCIÓN EN EXCAVACIONES PROFUNDAS. XVI PAN-AMERICAN CONFERENCE ON SOIL MECHANICS AND GEOTECHNICAL ENGINEERING, NOVEMBER.

MARIACHI, D., CHAN, C., & SEED, H. B. (1972). EVALUATION OF PROPERTIES OF ROCKFILL MATERIALS. JOURNAL OF THE SOIL MECHANICS AND FOUNDATIONS, DIVISION 9, 117–141.

MEDINA DÍAZ, C. L. (2002). ESTUDIO DEL EFECTO ARCO APLICADO A PROBLEMAS DE INGENIERÍA GEOTÉCNICA.

MONONOBE, N., & MATSUO, H. (1929). ON THE DETERMINATION OF EARTH PRESSURE DURING EARTHQUAKES. PROCEEDINGS OF WORLD ENGINEERING CONGRESS, VOL. 9, 177–185.

ORTIGOSA, P. (2001). ENTIBACIONES GRAVA SANTIAGO ORTIGOSA. IN ENTIBACIONES EN GRAVA.

OSTERMAYER, H., & RANKE, A. (1968). BEITRAG ZUR STABILITÄTSUNTERSUCHUNG MEHRFACH VERANKERTER BAUGRUBENUMSCHLIESSUNGEN. DIE BAUTECHNICK 45, N° 10, 341.

PAIK, K. H., & SALGADO, R. (2003). ESTIMATION OF ACTIVE EARTH PRESSURE AGAINST RIGID RETAINING WALLS CONSIDERING ARCHING EFFECTS. GEOTECHNIQUE, 53(7), 643–653. HTTPS://DOI.ORG/10.1680/GEOT.2003.53.7.643

PARDO, G. (2013). ESTUDIO EXPERIMENTAL Y NUMERICO DEL EFECTO DE ARCO.

PEDRO ORTIGOSA, & EUGENIO RETAMAL. (1994). SOCALZADOS Y ENTIBACIONES EN LA GRAVA DE SANTIAGO. IN INTERNATIONAL CONFERENCE ON SOIL MECHANICS AND FOUNDATION ENGINEERING (PP. 1–16).

RADDATZ, D., & TAIBA, O. (2017). ANCHORED PILES IN SANTIAGO'S GRAVEL: MODELING RESULTS FOR DISPLACEMENT CURVE. REVISTA DE LA CONSTRUCCION, 16(3), 457–467.

ROZIC, C. (2012). MODELACIÓN E INSTRUMENTACIÓN DE LAS PILAS DE ENTIBACIÓN DEL MODELACIÓN E INSTRUMENTACIÓN DE LAS PILAS DE ENTIBACIÓN DEL PROYECTO BEAUCHEF PONIENTE.

SÁEZ, E., & LEDEZMA, C. (2010). EVALUACIÓN DE LOS EMPUJES SÍSMICOS SOBRE ENTIBACIÓN DISCONTINUA EN EXCAVACIONES: ESTUDIO NUMÉRICO. CONGRESO CHILENO DE SISMOLOGÍA E INGENIERÍA ANTISÍSMICA. X JORNADAS.

SÁEZ, E., & LEDEZMA, C. (2012). EARTHQUAKE-INDUCED PRESSURES ON DISCONTINUOUS PILING SUPPORT ON SANTIAGO GRAVEL. SOIL DYNAMICS AND EARTHQUAKE ENGINEERING, 41, 72–83. HTTPS://DOI.ORG/10.1016/J.SOILDYN.2012.05.007

SALAS, F. (2017). MONITORING AND DYNAMIC ANALYSIS OF A DISCONTINUOUS PILE-SUPPORTED DEEP EXCAVATION IN SATIAGO GRAVEL. DECEMBER.

SALAS, FELIPE, SÁEZ, E., OVALLE, C., & FERNÁNDEZ, J. M. (2019). ANÁLISIS DINÁMICO DE UNA EXCAVACIÓN PROFUNDA CONTENIDA MEDIANTE PILOTES ANCLADOS EN LA GRAVA DE SANTIAGO. OBRAS Y PROYECTOS, 25, 76–82. HTTPS://DOI.ORG/10.4067/S0718-28132019000100076

VÁSQUEZ, A. (2018). ANÁLISIS DE SINGULARIDAD EN ENTIBACIONES DE PILAS DISCONTINUAS.

ZHU, F. BIN, MIAO, L. C., GU, H. DA, & CHENG, Y. H. (2013). A CASE STUDY ON BEHAVIORS OF COMPOSITE SOIL NAILED WALL WITH BORED PILES IN A DEEP EXCAVATION. JOURNAL OF CENTRAL SOUTH UNIVERSITY, 20(7), 2017–2024.

BENZ, T. (2007). SMALL-STRAIN STIFFNESS OF SOILS AND ITS NUMERICAL CONSEQUENCES. IN THE UNIVERSITY OF STUTTGART.

BOLDRINI, S., & LÓPEZ, F. (2014). DISEÑO E INSTRUMENTACIÓN EN ENTIBACIÓN MEDIANTE PILOTES ANCLADOS EN LA GRAVA DE SANTIAGO.

CHEN, C. Y., & MARTIN, G. R. (2002). SOIL - STRUCTURE INTERACTION FOR LANDSLIDE STABILIZING PILES. COMPUTERS AND GEOTECHNICS, 29(5), 363–386.

KHATAMI, H., DENG, A., & JAKSA, M. (2019). AN EXPERIMENTAL STUDY OF THE ACTIVE ARCHING EFFECT IN SOIL USING THE DIGITAL IMAGE CORRELATION TECHNIQUE. COMPUTERS AND GEOTECHNICS, 108(JANUARY), 183–196. HTTPS://DOI.ORG/10.1016/J.COMPGEO.2018.12.023

KORT, I., MUSANTE, H., & FAHRENKROG, C. (1979). IN-SITU MECHANICAL PROPERTIES MEASUREMENTS OF GRAVELLY SOIL USED IN AN INTERACTION AND FOUNDATION MODEL FOR THE SANTIAGO METRO. 6TH PANAMERICAN CONFERENCE ON SOIL MECHANICS AND FOUNDATION ENGINEERING, 217–224.

LÓPEZ, S., & SANHUEZA, C. (2019). ANÁLISIS DE LA DISTRIBUCIÓN DE EMPUJES DE SUELOS SOBRE ESTRUCTURAS DE CONTENCIÓN EN EXCAVACIONES PROFUNDAS. XVI PAN-AMERICAN CONFERENCE ON SOIL MECHANICS AND GEOTECHNICAL ENGINEERING, NOVEMBER.

MEDINA DÍAZ, C. L. (2002). ESTUDIO DEL EFECTO ARCO APLICADO A PROBLEMAS DE INGENIERÍA GEOTÉCNICA.

ORTIGOSA, P. (2001). ENTIBACIONES GRAVA SANTIAGO ORTIGOSA. IN ENTIBACIONES EN GRAVA.

PAIK, K. H., & SALGADO, R. (2003). ESTIMATION OF ACTIVE EARTH PRESSURE AGAINST RIGID RETAINING WALLS CONSIDERING ARCHING EFFECTS. GEOTECHNIQUE, 53(7), 643–653. HTTPS://DOI.ORG/10.1680/GEOT.2003.53.7.643

PARDO, G. (2013). ESTUDIO EXPERIMENTAL Y NUMERICO DEL EFECTO DE ARCO.

PEDRO ORTIGOSA, & EUGENIO RETAMAL. (1994). SOCALZADOS Y ENTIBACIONES EN LA GRAVA DE SANTIAGO. IN INTERNATIONAL CONFERENCE ON SOIL MECHANICS AND FOUNDATION ENGINEERING (PP. 1–16).

RADDATZ, D., & TAIBA, O. (2017). ANCHORED PILES IN SANTIAGO'S GRAVEL: MODELING RESULTS FOR DISPLACEMENT CURVE. REVISTA DE LA CONSTRUCCION, 16(3), 457–467.

ROZIC, C. (2012). MODELACIÓN E INSTRUMENTACIÓN DE LAS PILAS DE ENTIBACIÓN DEL MODELACIÓN E INSTRUMENTACIÓN DE LAS PILAS DE ENTIBACIÓN DEL PROYECTO BEAUCHEF PONIENTE.

SÁEZ, E., & LEDEZMA, C. (2010). EVALUACIÓN DE LOS EMPUJES SÍSMICOS SOBRE ENTIBACIÓN DISCONTINUA EN EXCAVACIONES: ESTUDIO NUMÉRICO. CONGRESO CHILENO DE SISMOLOGÍA E INGENIERÍA ANTISÍSMICA. X JORNADAS.

SALAS, F. (2017). MONITORING AND DYNAMIC ANALYSIS OF A DISCONTINUOUS PILE-SUPPORTED DEEP EXCAVATION IN SATIAGO GRAVEL. DECEMBER.

VÁSQUEZ, A. (2018). ANÁLISIS DE SINGULARIDAD EN ENTIBACIONES DE PILAS DISCONTINUAS.

ZHU, F. BIN, MIAO, L. C., GU, H. DA, & CHENG, Y. H. (2013). A CASE STUDY ON BEHAVIORS OF COMPOSITE SOIL NAILED WALL WITH BORED PILES IN A DEEP EXCAVATION. JOURNAL OF CENTRAL SOUTH UNIVERSITY, 20(7), 2017–2024.

11 Appendix

1.1 Detail of Construction Phases

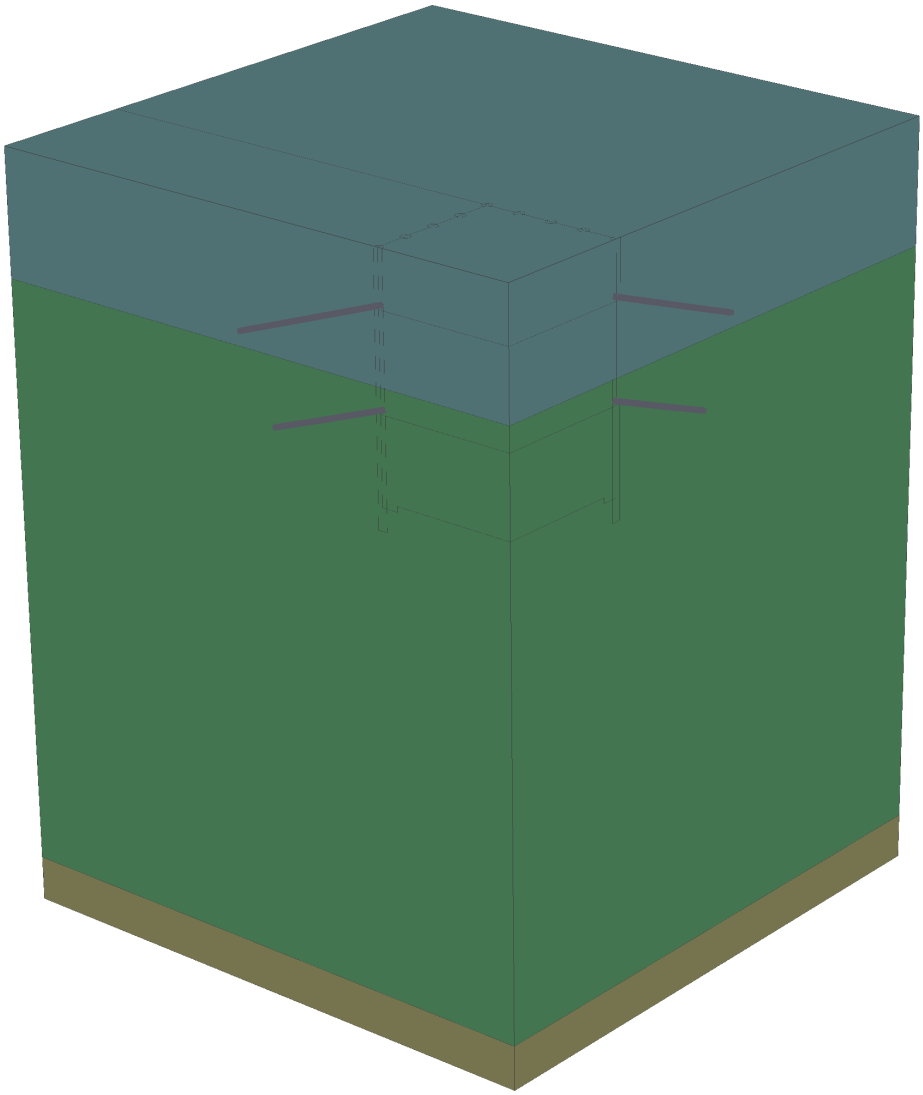

Figure 34 Stage 1: Initial phase.

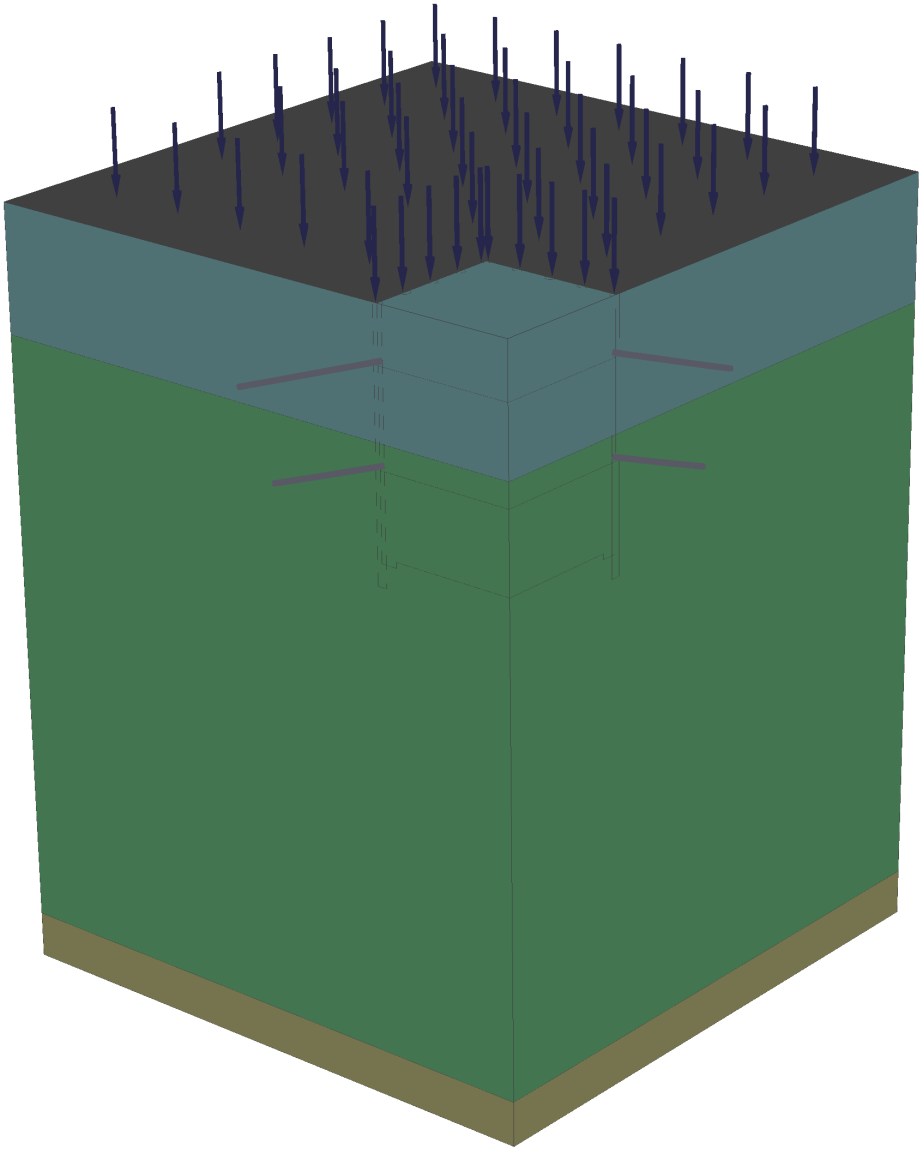

Figure 35 Stage 2: Application of the surcharge load (12 kPa).

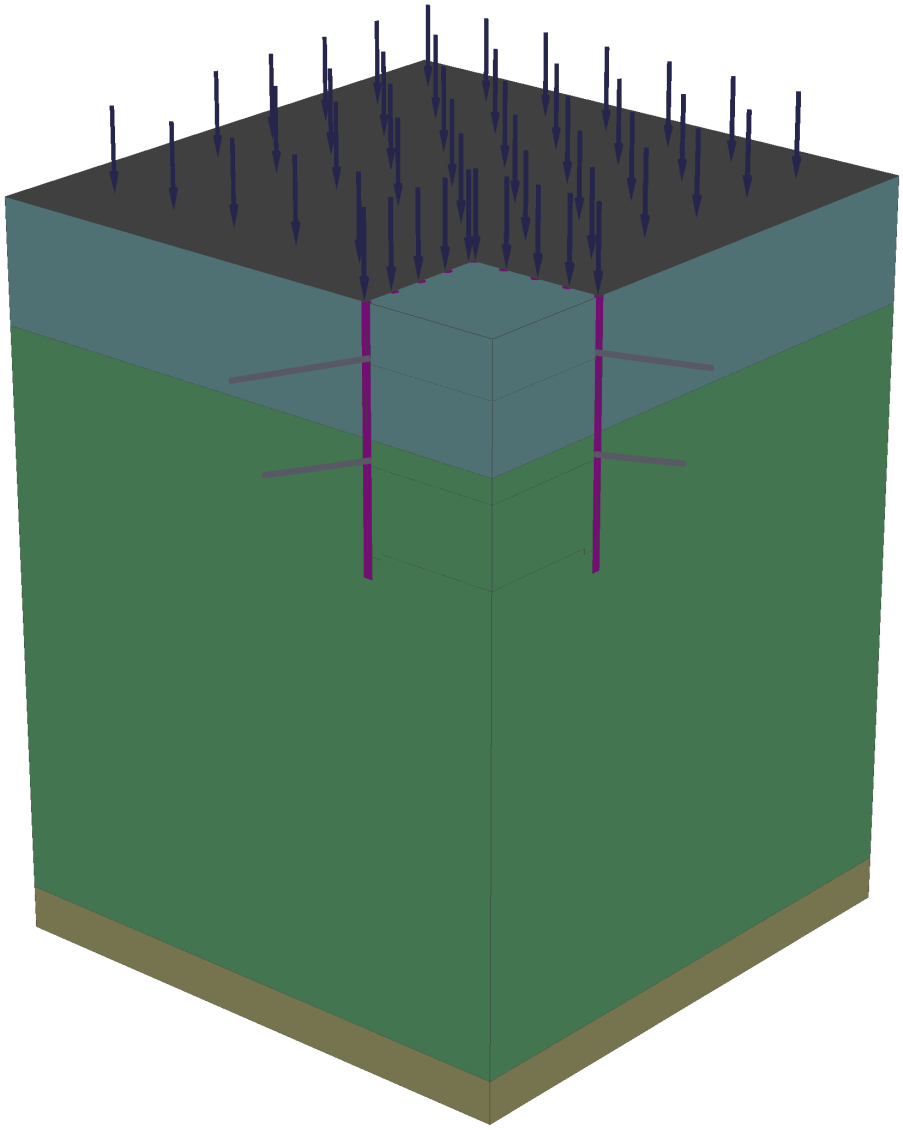

Figure 36 Stage 3: Installation of the pile.

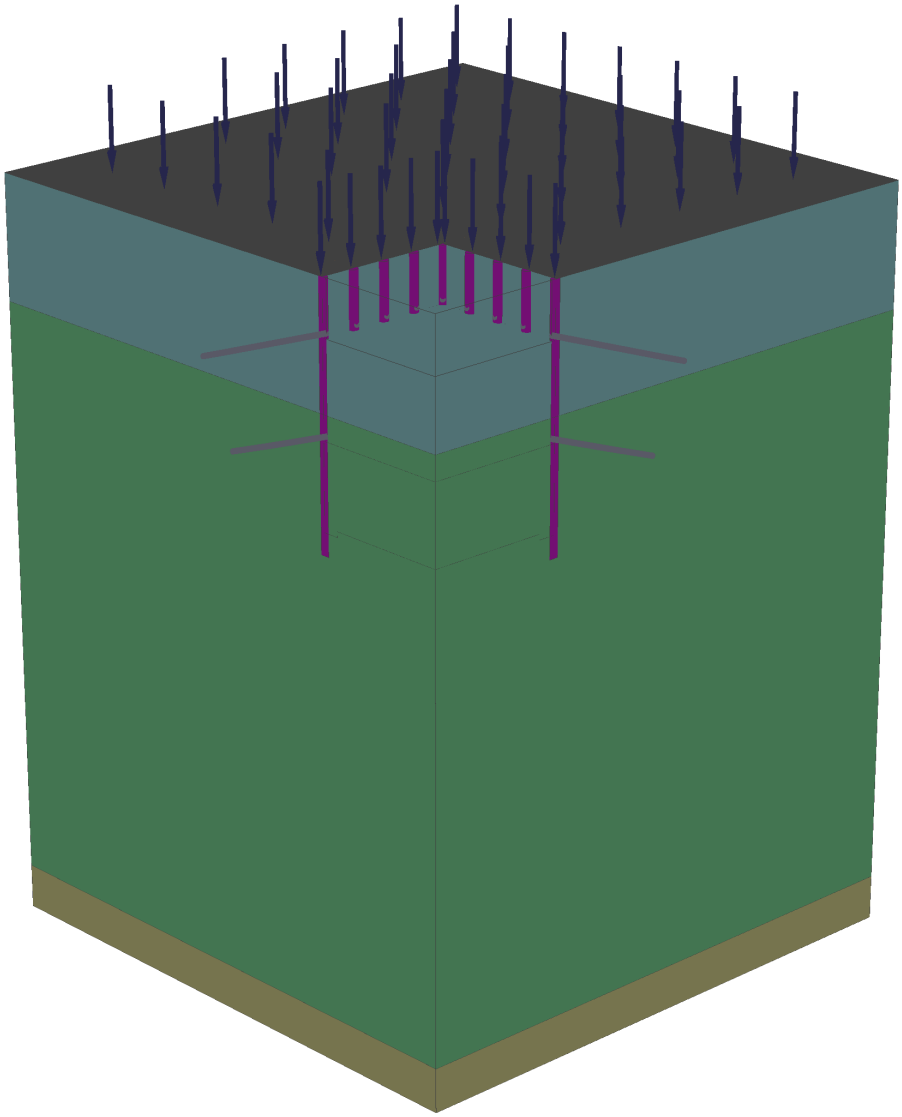

Figure 37 Stage 4: First excavation.

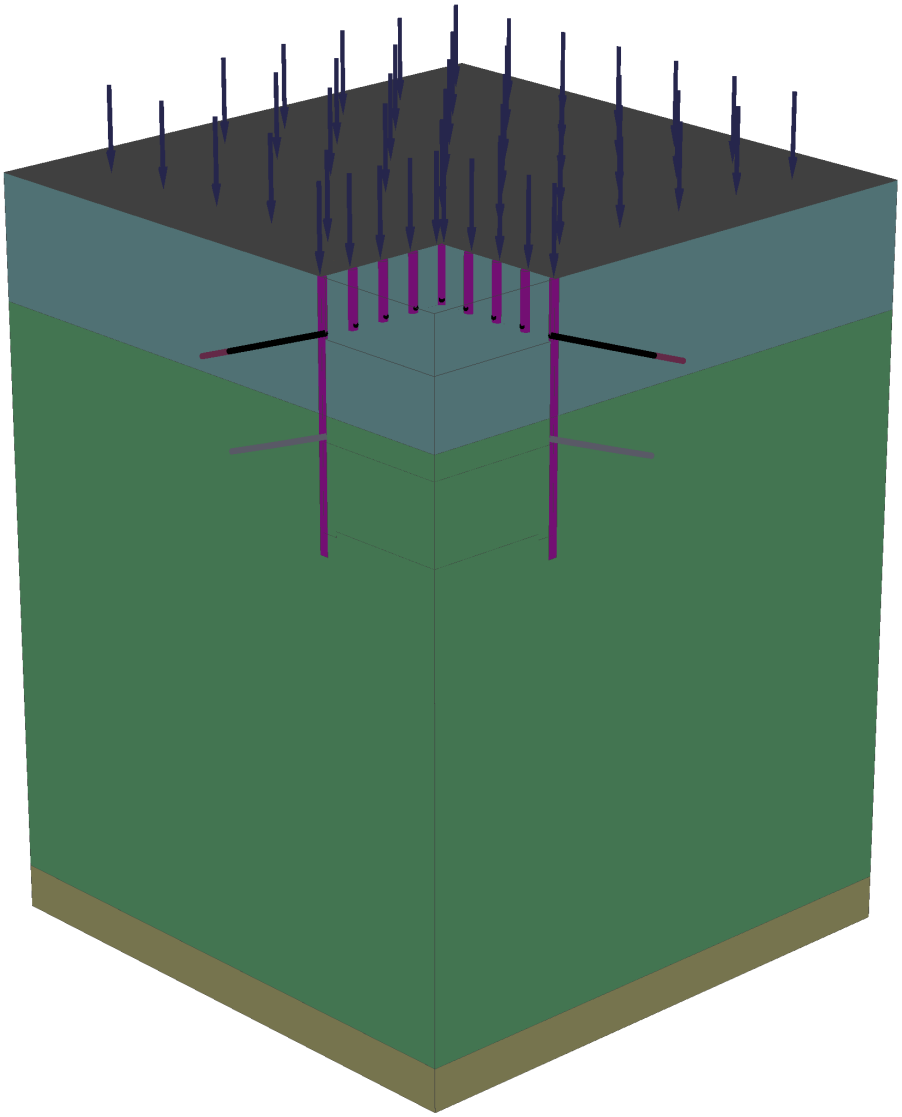

Figure 38 Stage 5: Installation and pre-stressing of the first anchor line.

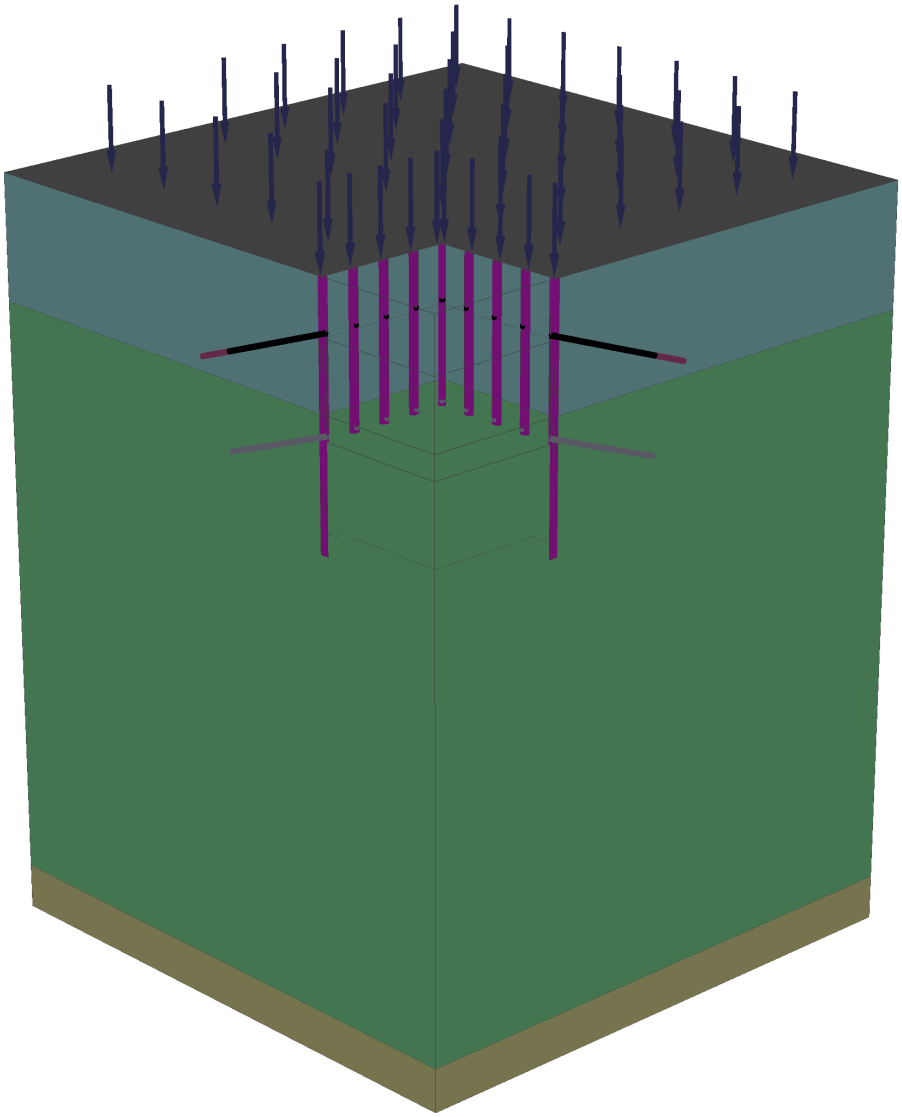

Figure 39 Stage 6: Second excavation.

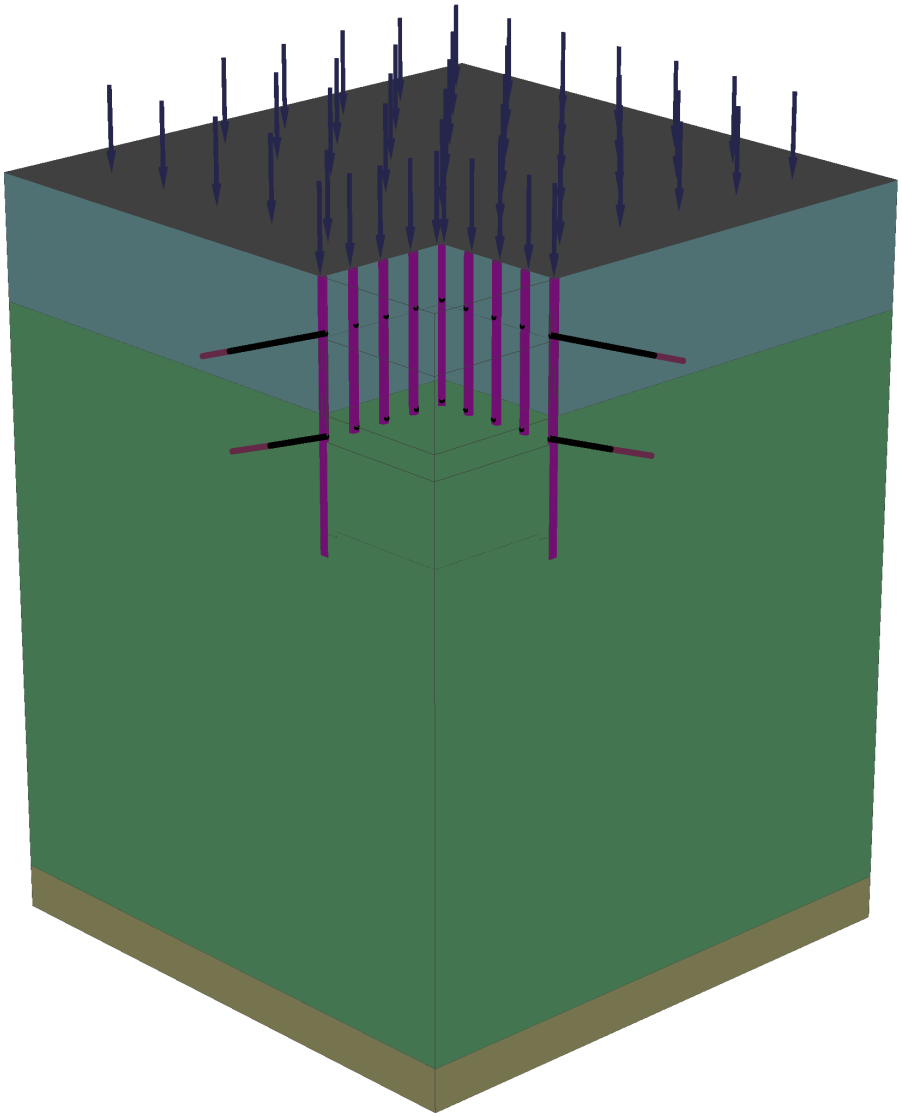

Figure 40 Stage 7: Installation and pre-stressing of the second anchor line.

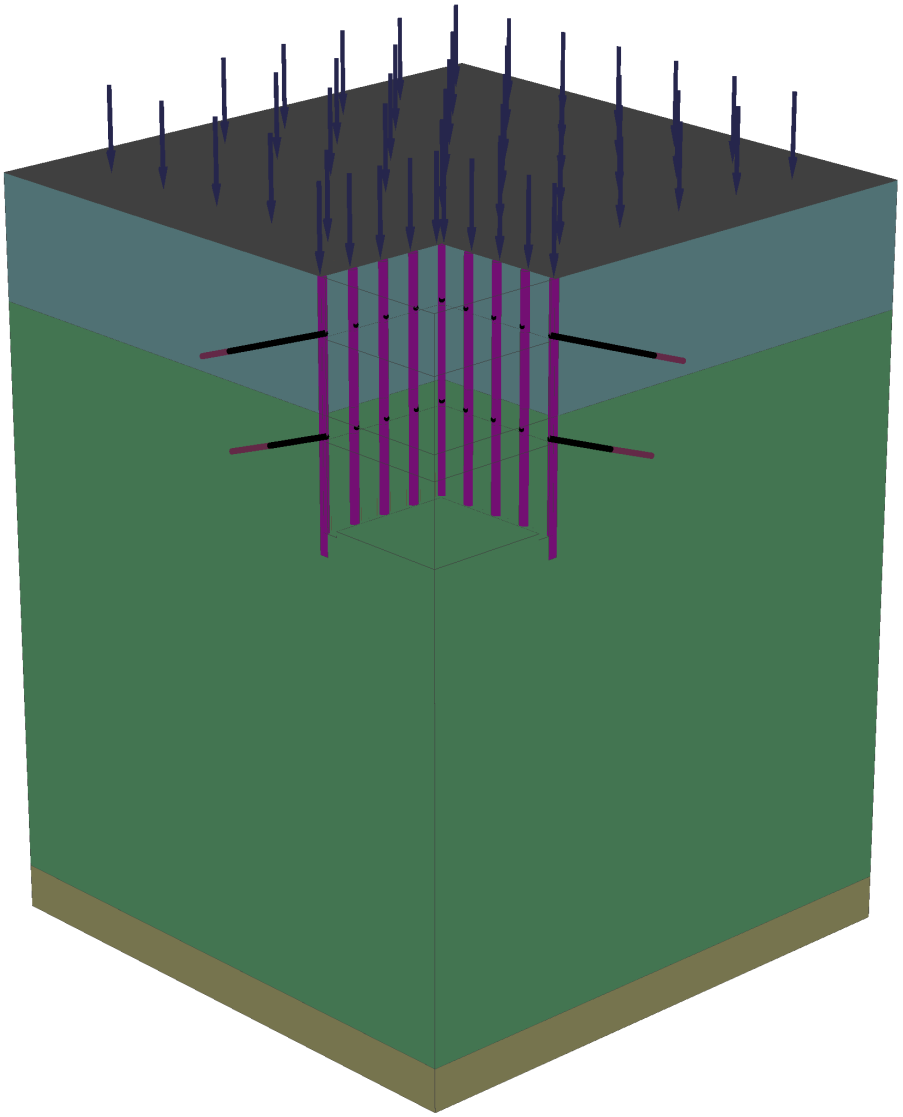

Figure 41 Stage 8: Excavation until the foundation seal level.

1.2 2D Section View of Pile-Anchor Configuration

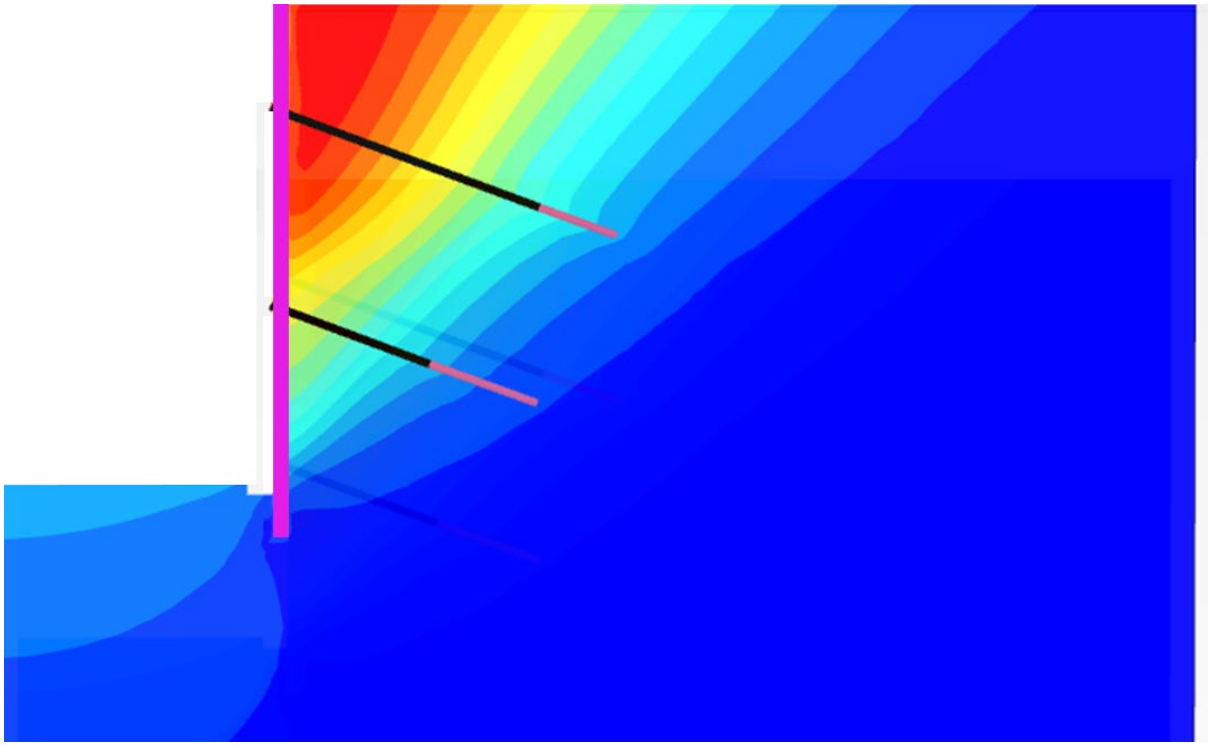

Figure 42 2D Section View of Pile-Anchor Configuration, static stage 8.

1.3 Dynamic Displacement in the X and Y Directions at the Pile Head

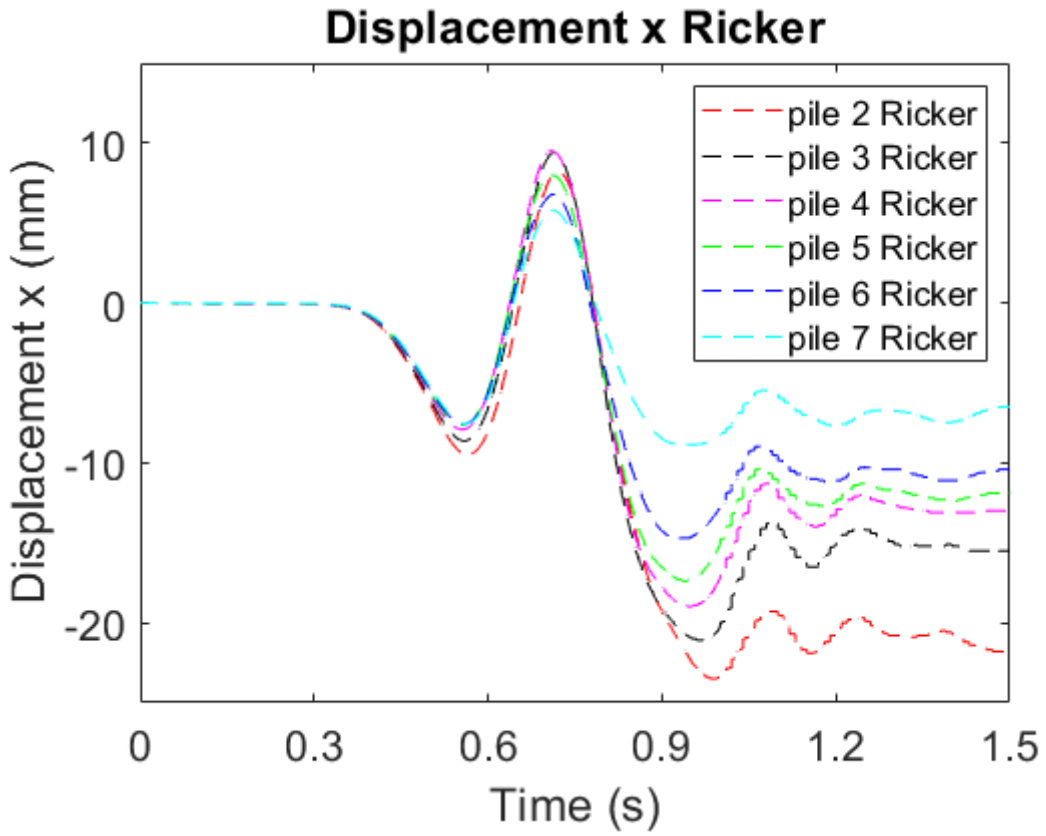

Figure 43 Dynamic displacement in x direction for Group 1. W-S input.

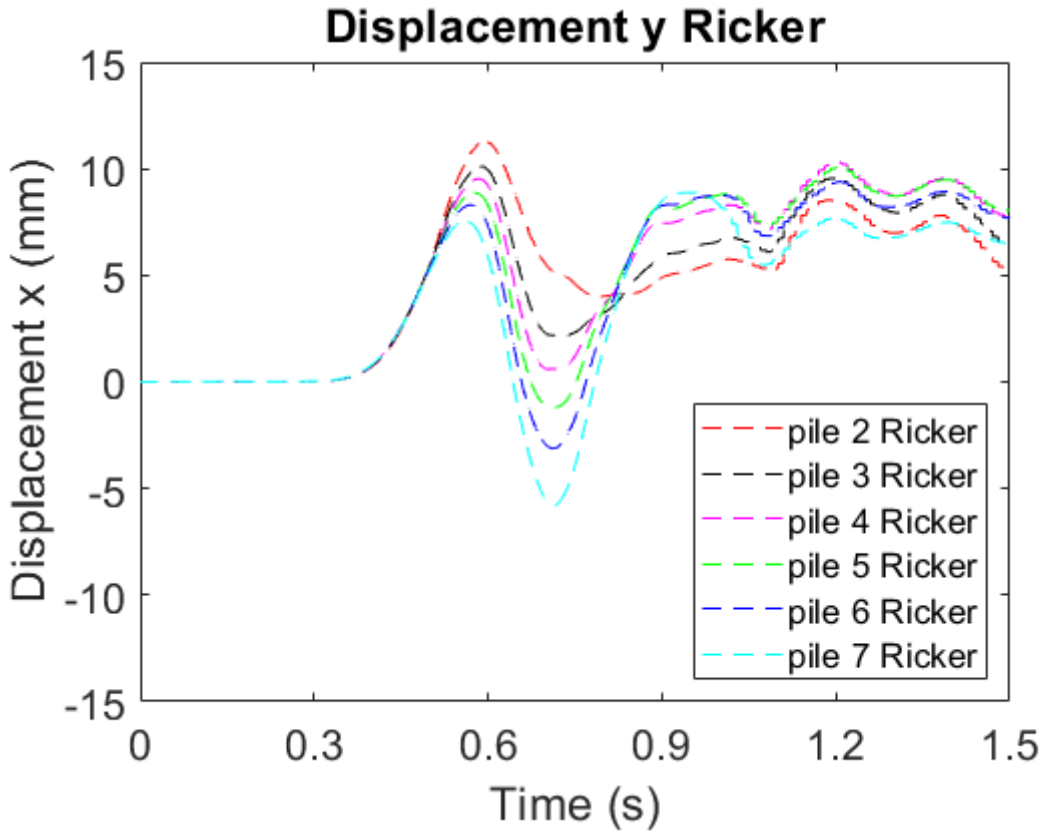

Figure 44 Dynamic displacement in y direction for Group 1. RW-S input.

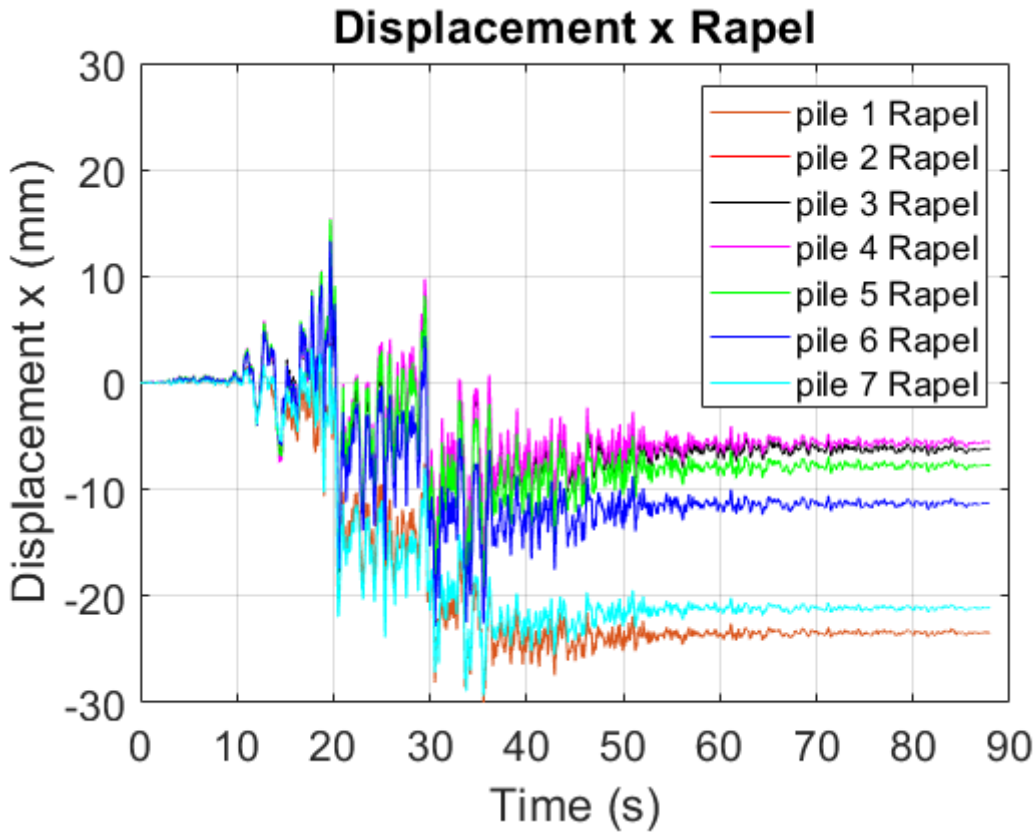

Figure 45 Dynamic displacement in x direction for Group 1. Rapel earthquake input.

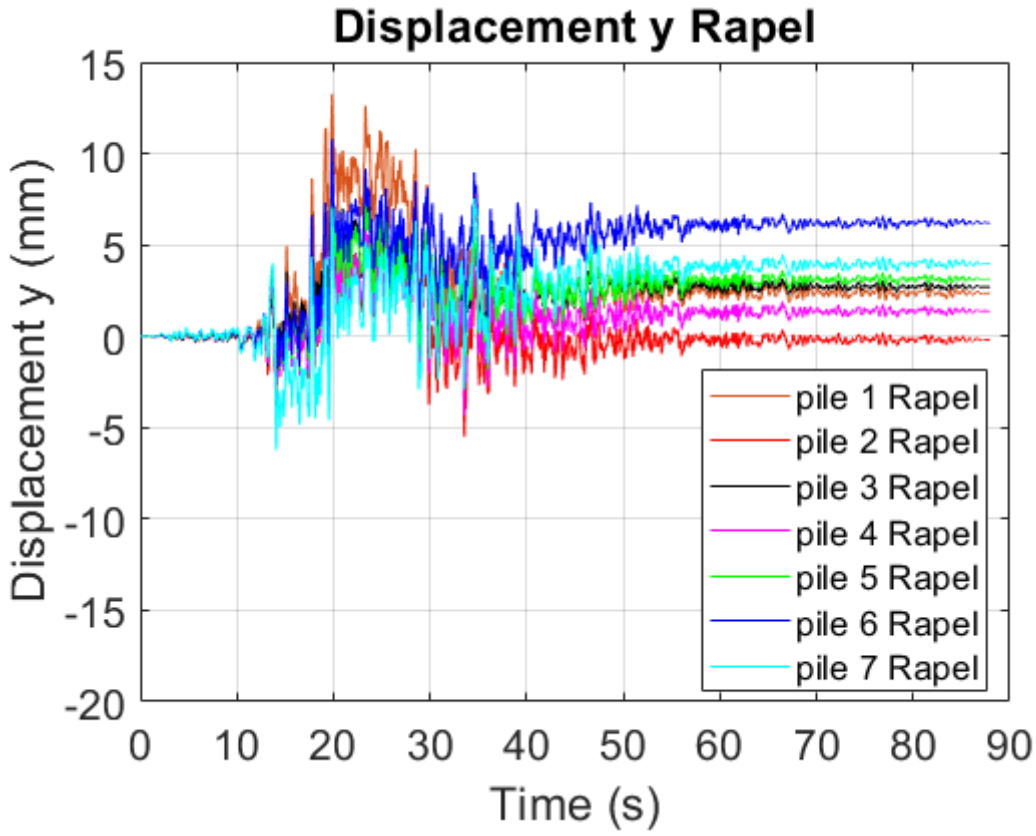

Figure 46 Dynamic displacement in y direction for Group 1. Rapel earthquake input.

1.4 Dynamic Soil Pressure

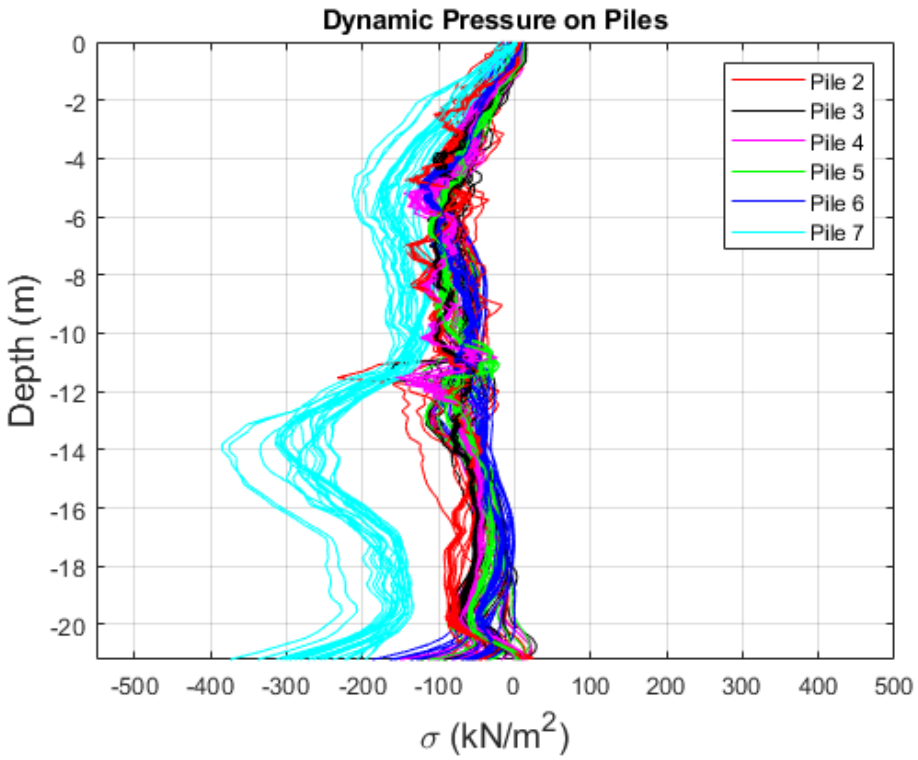

Figure 47 Dynamic soil pressure for Group 1. RW-S input.

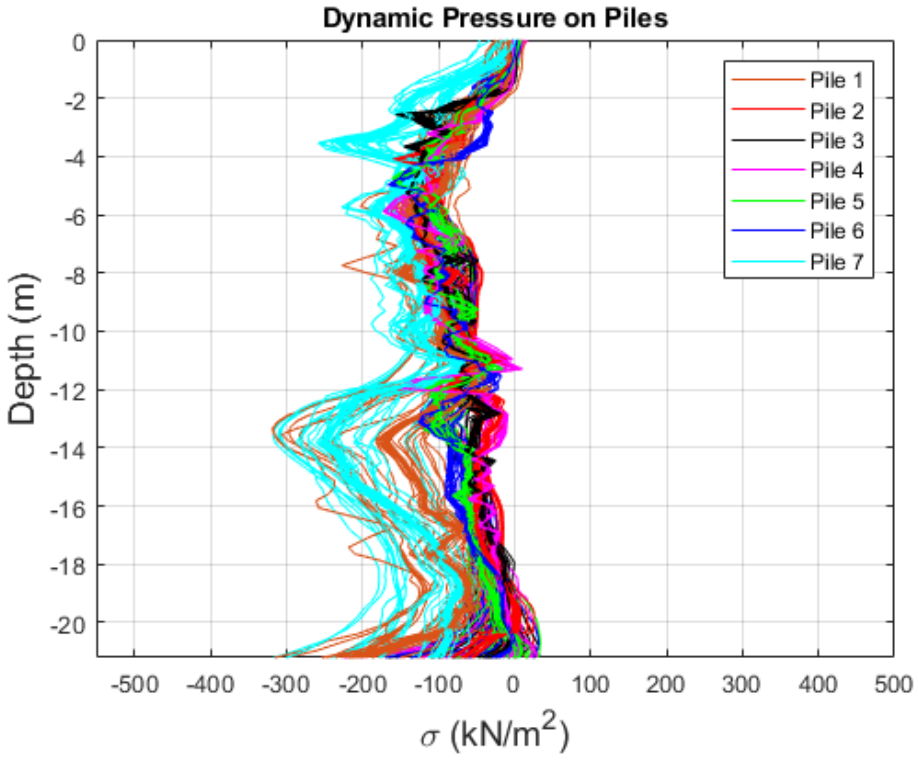

Figure 48 Dynamic soil pressure for Group 1. Rapel earthquake input.

1.5 Hardening Soil with Small-Strains Stiffness Model

This constitutive model is based on the usual Hardening Soil (isotropic hardening), but two more parameters are included that allow modeling the range of shear deformation in which the soil behaves linearly.

Below, a brief description of the constitutive model is presented, based on the PLAXIS 3D Manual and the research by Salas (2017).

The usual Hardening Soil Model (isotropic hardening) is based on a non-linear stress-strain behavior given by a hyperbolic function proposed by Duncan-Chang (1970), by means of the equation (2):

$$-\varepsilon_1 = \frac{1}{E_i}\frac{q}{1-\frac{q}{q_a}} \qquad for: q < q_f \tag{2}$$

Where q_a:is the asymptotic shear stress value and E_i the initial stiffness.E_i is related to E_{50} by the equation (3):

$$E_i = \frac{2E_{50}}{2-R_f} \tag{3}$$

The parameter E_{50} is the secant stiffness modulus at 50% of the value of q_a for primary load, dependent on the confinement stress and is given by the equation (4):

$$E_{50} = \left(\frac{c\ cos\ (\varphi - \sigma_3'\ sin(\varphi)}{c\ cos\ cos\ (\varphi)\ + p'_{ref}\ sin\ (\varphi)}\right)^m \tag{4}$$

Where E_{50}^{ref} is the reference stiffness modulus according to a reference confining pressure (p'_{ref}), while the stiffness modulus (E_{50}) depends on the principal stress (σ'_3) applied. The magnitude of stress dependence is given by the factor *m*, which can be calibrated using the referential shear modulus (G_{ref}) y p'_{ref} to obtain the shear modulus at any effective confining pressure p' , by means of the following equation (5):

$$G(p') = G_{ref}\left(\frac{p'}{p'_{ref})}\right)^m \tag{5}$$

The ultimate deviator stress (q_f) and the asymptotic shear stress value (q_a) shown in the previous formulas are defined by the equation (6) and (7):

$$q_f = (c\ cot\ cot\ (\varphi)\ - \sigma'_3)\frac{2\ sinsin\ sin\ (\varphi)}{1-sinsin\ sin\ (\varphi)} \tag{6}$$

$$and \quad q_a = \frac{q_f}{R_f} \tag{7}$$

The previous expression for q_f is derived from the Mohr-Coulomb failure criterion, which involves the parameters *c* and φ. As soon as q reaches the value q_f, the criterion of plastic failure is satisfied, same as in the Mohr-Coulomb model. For unloading and reloading, another dependent effort module is used, and its formula is shown below in the equation (8):

$$E_{ur} = E_{ur}^{ref}\left(\frac{c\ cos\ cos\ (\varphi)\ - \sigma'_3\ sin\ sin\ (\varphi)}{c\ cos\ cos\ (\varphi)\ +\ p'_{ref} sin\ (\varphi)}\right)^m \tag{8}$$

Where E_{ur}^{ref} is the reference stiffness modulus for reload and unload corresponding to p'_{ref}.

The hyperbolic relationship described in the previous paragraphs can be seen graphically in Figure 49.

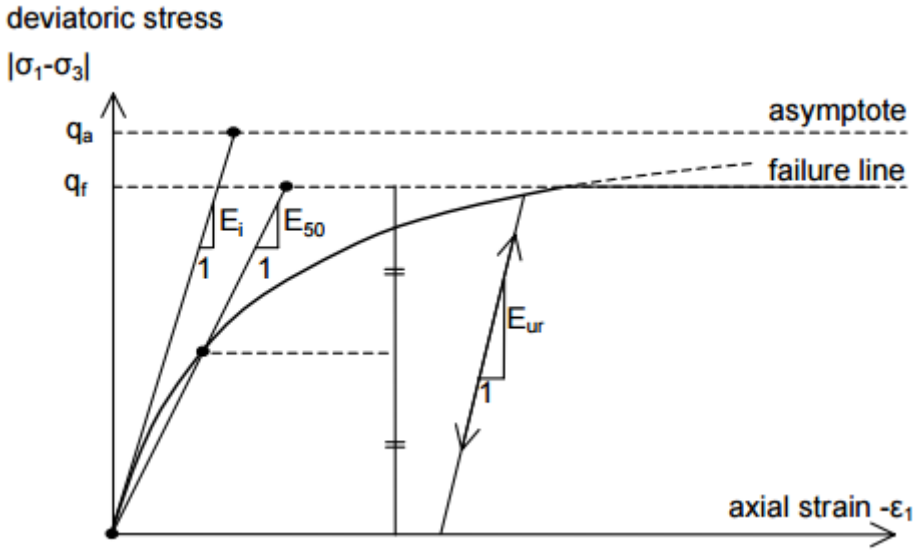

Figure 49 The hyperbolic relationship. (Plaxis3D® Reference Manual)

This model incorporates the deviatoric and isotropic hardening mechanism. Deviatoric hardening describes yielding shear as shows in the equation (9):

$$f = \underline{f} - \gamma^p \tag{9}$$

Where $\underline{f}$ is the stress function and γ^p is the accumulated plastic shear strain. As for the plastic deformations, they are given by the following equation (10):

$$-\varepsilon_1^e = \frac{q}{E_{ur}} \quad and \quad -\varepsilon_2^e = -\varepsilon_3^e = -\upsilon_{ur}\frac{q}{E_{ur}} \tag{10}$$

Where υ_{ur} is the Poisson' s ratio of reload and unload

For a given state of γ^p, the yield condition $f = 0$, can be visualized in the $p' - q$ plane since γ^p can be associated with mobilized friction as well as mobilized shear stress.

The model computes the volumetric strain using the following hardening flow rule presented by the equation (11):

$$\dot{\varepsilon}_v^p = sin\ sin\ (\psi_m)\dot{\gamma}^p \tag{11}$$

Where ψ_m is the mobilized dilatancy angle dependent on the mobilized friction and the ultimate state of the internal friction angle.

The isotropic hardening mechanism is represented in the form of a surface cap acting as a pre-consolidation pressure threshold, where plastic deformation is expected to occur beyond that limit, characterizing a normally consolidated soil state. A model without an isotropic hardening mechanism overestimates soil stiffness and consequently underestimates deformations.

In the principal stress space, the yield surface of the model presented in Figure 50 corresponds to the classical hexagonal form of the Mohr-Coulomb failure criterion and its yield "cap".

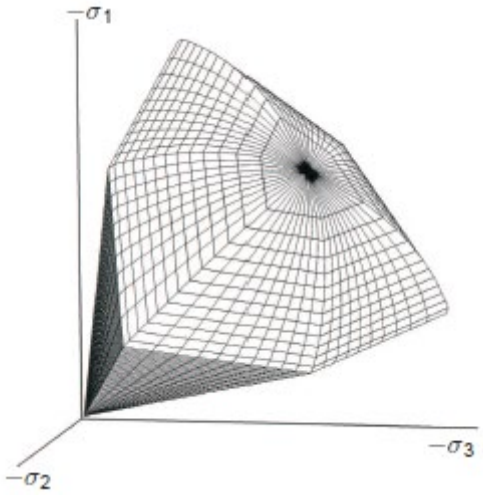

Figure 50 Hardening Soil Model failure criterion. (Plaxis3D® Reference Manual)

To simulate the behavior of dilatant materials when they reach a state of critical density after extensive shearing, the model also incorporates a dilatancy limit. For this, the initial and maximum void ratio should be provided as input parameters.

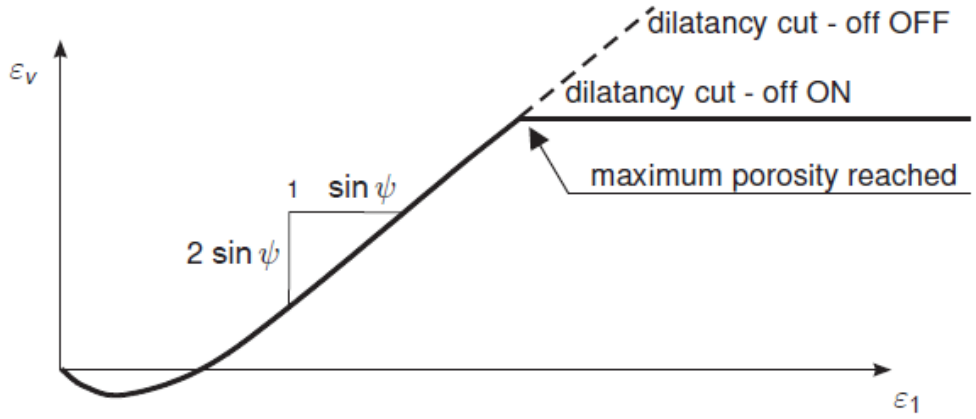

Figure 51 Dilatancy limit behavior used in HS-Small model. (Plaxis3D® Reference Manual)

the Hardening Soil Model for small deformations (HS-Small), unlike the common HS model, assumes an elastic behavior during unloading and reloading. Although this behavior is only valid for a very small range of deformations. It is known that, as the amplitude of the deformation increases, the soil stiffness decreases non-linearly. HS-small offers the possibility of incorporating the soil stiffness degradation for small deformations and its non-linear dependence on the amplitude of the deformations. It uses almost entirely the same parameters as HS-standard, introducing two additional parameters:

a) Very small-strain shear modulus G_0 (or G_{max})

b) The shear strain level at which the secant shear modulus G_s is reduced to about 70% of G_0: $\gamma_{0.7}$

To describe the hyperbolic law of stiffness for small deformations, HS-Small uses the Hardin & Drnevich (1972) relation, modified by Santos & Correa (2001) to incorporate the limit of small deformations. The resulting expression is shown by the equation (12):

$$\frac{G_s}{G_0} = \frac{1}{1+a\left|\frac{\gamma}{\gamma_{0.7}}\right|} \quad where,\ a = 0.385 \tag{12}$$

The model also adopts Masing's rule to describe the hysteretic behavior of the material in unload/reload cycles.

The summary of the necessary parameters to use the HS-Small model are listed in Table 11:

Table 11 Necessary parameters to use the HS-Small model.

Parameter	Units	Description
m	-	Power for stress-level dependency of stiffness
E_{50}^{ref}	kPa	Secant stiffness in standard drained triaxial test
E_{oed}^{ref}	kPa	Tangent stiffness for primary oedometer loading
E_{ur}^{ref}	kPa	Unloading/reloading stiffness from drained triaxial test
G_0^{ref}	kPa	Reference shear modulus for p'_{ref} at very smalls strains ($\varepsilon < 10^{-6}$)
$\gamma_{0.7}$	-	Threshold shear strain at which $G_s = 0.7G_0$
c'	kPa	Effective cohesion
φ'	°	Effective angle of internal friction
ψ	°	Angle of dilatancy
σ_t	kPa	Tension cut-off and tensile strength
ν_{ur}	-	Poisson's ratio for unloading/reloading
R_f	-	Failure ratio $\frac{q}{q_a}$(Default $R_f = 0.9$)
K_0^{nc}	-	K_0 −value for normal consolidation
c_{inc}	$\frac{kN}{m^3}$	Incremental cohesion with depth
$e_{initial}$	-	Initial void ratio
e_{max}	-	Maximum void ratio